Spring 5-19-2017

An Experimental Study in the Hydroelastic Response of an Aluminum Wedge in Drop Tests

Jonathan R. Eastridge
jeastrid@uno.edu

Recommended Citation

Eastridge, Jonathan R., "An Experimental Study in the Hydroelastic Response of an Aluminum Wedge in Drop Tests" (2017). *University of New Orleans Theses and Dissertations*. 2317.
https://scholarworks.uno.edu/td/2317

An Experimental Study in the Hydroelastic Response of an Aluminum Wedge in Drop Tests

A Thesis

Submitted to the Graduate Faculty of the
University of New Orleans
in partial fulfillment of the
requirements for the degree of

Master of Science
in
Engineering
Naval Architecture and Marine Engineering

by

Jonathan R. Eastridge

B.S. University of New Orleans, 2016

May, 2017

Acknowledgments

First of all, I acknowledge that I am contributing to a decades-old topic, and I wish only to offer my thoughts and efforts.

The Louisiana State Board of Regents (Industrial Ties Research Subprogram [LEQSF (2015-18)-RD-B-09]) should be thanked for sponsoring this project. Also, this research would not have been possible without the skill and generosity of Metal Shark Boats in providing the experimental model and housing rig.

Many thanks are due to my advisor, Dr. Brandon Taravella, for his guidance throughout my university studies and especially this research. His patience and insight are priceless, and I look forward to further collaboration with him.

I would also like to thank Dr. Christine Ikeda, the former PI of this project and professor at UNO, for her efforts and encouragement in getting me started with this project. Without her I might not have had the opportunity to do this work.

Dr. Lothar Birk and Dr. Nikolaos Xiros, also deserve thanks for agreeing to participate in my thesis committee. They have helped me tremendously during my time at UNO.

The UNO School of NAME staff members Ryan Thiel and George Morrissey participated invaluably throughout, and I am grateful for their help. My colleague, Jordan Castillo, with whom I collaborated extensively on this project, should also be thanked for helping even beyond the scope of his obligations.

Thanks also to Soledad Calderón and Dylan Cuvelier for agreeing to the DIC code project in ENEE 6581/CSCI 6990. I could not have finished it alone. Our deliverables for that project evolved into the S-DIC code used to accomplish this thesis.

My family and friends must be among the most supportive and loving people on earth. They are too many to name, but I am most grateful for them. Philippians 1:3.

Table of Contents

List of Figures

List of Tables

Abstract

Slamming of marine planing craft is expected to arise due to the high speed nature of their operating conditions. High hydrodynamic forces are inevitably induced causing the shell plating to deflect, which in turn can influence the flow physics surrounding the hull. In order to study the hull's hydroelastic response due to a slamming event, *wedge drop experiments* were performed with an aluminum wedge of 57 inches in length, 47 inches in breadth, and 20° deadrise with $1/4$ in. thick unstiffened bottom panels. The elastic behavior of the hull plating was measured via two methods. The first method uses strain gages to analyze the wedge's deadrise panel deflections, and the second method is a Stereoscopic-Digital Image Correlation (S-DIC) technique. In the present investigation, an S-DIC code has been developed and utilized to study the deflections and to advance the capabilities of future research. Comparisons are made between the methods and also with theoretical studies. The deflections measured are approximately 0.1 in. on a panel spanning 24.5 inches, and the predictions made using S-DIC and strain gages differ by approximately 23%.

Keywords:

naval architecture, marine engineering, hydroelasticity, hydrodynamics, planing, wave slamming, wedge drop experiment

Chapter 1

Introduction

Marine vessels must be designed to operate in a dynamic and complex environment, and surface ships in particular must be prepared to deal with the consequences associated with the water's free surface. This includes the hazardous nature of waves and high accelerations. Any dynamic problem combining the complexities of fluid flow with the geometrical constraints of a body in contact with the fluid is called a *fluid-structure interaction* (FSI) problem. As the body of interest deforms – a property known as *hydroelasticity* – when interacting with the fluid, the FSI problem becomes dependent on the object's level of elasticity because the flow physics will vary as the body changes shape. Bottom plating on a ship experiencing elastic deformation will return to its original shape when the load is removed. However, rough sea conditions can produce loads during severe pitching motions that will cause the plating to experience inelastic deformation, and further loading consequentially leads to failure. Therefore, an understanding of the hydroelastic response of a marine vessel in its operating conditions is crucial to a designer's ability to produce an effective and safe design.

Hydroelasticity generally refers to the modification of the flow physics of water interacting with a deformable material during a slamming event. Slamming of hulls occurs when waves with high propagation speed impact the shell plating or when a ship with a flat bottom enters the water with high vertical velocity. This is frequently found to be the case e.g. for planing hulls that are designed to travel at high forward speeds. A planing vessel with cross sections characterized by low deadrise angles and flat shell plating such as the one seen in Figure 1.1 often experience slamming to a dangerous degree and is threatened in the integrity of its structural members. The heaving and pitching motions resulting from the impacts may also jeopardize the safety of the onboard personnel, machinery, and equipment.

Studying hydroelasticity is important for determining the conditions that introduce danger due to hydroelastic behavior. A thorough understanding of the relationship between structural response and flow physics facilitates overcoming the challenges associated with designing planing vessels. The primary challenge in planing boat design is identifying a structural arrangement that is light enough to permit planing and skimming without overly compromising strength. These decisions are equally important in the design of unmanned vessels that are meant to operate in adverse conditions at high Froude numbers [8].

Two approaches to studying hydroelasticity include computational hydrodynamics coupled with finite element analysis and experimentation. This thesis studies FSI problems and hydroelasticity experimentally and with comparisons to analytical codes [16]. For the accomplishment of this thesis, the experiments performed to study these phenomena are known as *wedge drop experiments.* An aluminum wedge was constructed and tested in slamming events during which data was collected to capture the shell plating response (details regarding the test model and experimental setup are provided in chapter 2). The analytical codes are based on Vorus' *flat cylinder theory* [18].

The purpose of this thesis is to report on the experimental findings in the hydroelastic response of an aluminum, symmetric, and wedge-shaped drop test cylinder and to study the possible influences of this behavior on the efficiency and motions of planing vessels experiencing slamming.

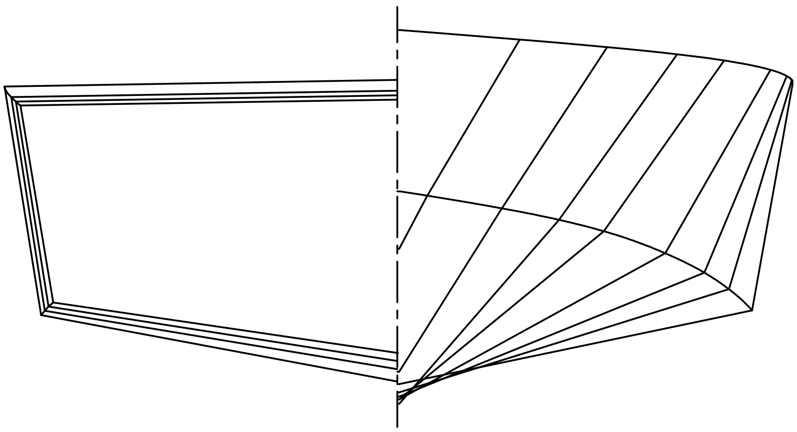

Figure 1.1: Body plan of a typical planing vessel

1.1 Background and Previous Work

The earliest theoretical study of rigid bodies entering the water and the associated dynamics was performed by Von Kármán [17] with the introduction of a momentum theory. His investigation included asymptotic solutions and focused on the prediction of forces acting on bodies experiencing slamming events for the purpose of analyzing the structural stresses local to the members absorbing the impact. The flow was assumed to be two-dimensional around a slender deadrise cylinder with vertical velocity.

Wagner [19] advanced Von Kármán's asymptotic solutions in analyzing the pressure distribution at the fluid-structure interface during water entry. His model was that of an infinitely long, expanding wedge with no chine, and a series expansion was used to define the contour geometry. However, jetrise – i.e. the development of a spray root – was included in the effects on the hydrodynamic pressures bringing the solution one step closer to reality than the analysis presented by Von Kármán. In reality (for ships), the maximum pressure occurs at the free surface/structure interface and moves outboard in the form of a spray root with generally decreasing magnitude, and Wagner was the first to include this behavior. Both Von Kármán's and Wagner's asymptotic solutions necessitate geometric similarity.

Vorus [18] developed a hydrodynamic model using ideal incompressible flow without gravitational effects to describe the flow physics occurring during a slamming event. He incorporated non-linear numerical time integration to solve for the hydrodynamic flow from the initial conditions at cylinder impact. The most significant contribution provided by Vorus is the introduction of a non-linear term in the kinematic boundary condition. Additionally, the models developed by Von Kármán and Wagner assume that the panels on the discretized body's surface are perfectly rigid and straight, while Vorus structured his model such that the rigid cylinder geometry could be varied simulating arbitrary cross sections. An important study that he performed includes an analysis of the flow associated with wedge cross-sections varying only in panel contour at constant impact velocity. Three contours were analyzed:

each contour begins with an initial deadrise angle of 20° at the keel and terminates at the hard chine with 10°, 20°, and 30° terminal angles. The contour terminating at 20° represents a linear (constant deadrise angle) contour. While varying this terminating angle parameter he studied the differences appearing in the solutions for keel pressure and vertical force coefficients. These discrepancies were used to highlight distinctions between fore and aft section responses of a planing hull and can be used more generally to describe the effects of the deadrise panel's hydroelastic response on the accompanying flow physics.

Faltinsen [4] studied the effects of hydroelasticity on slamming-induced structural stresses as a function of deadrise angle and impact velocity. His analysis incorporated the effects of structural vibrations. He noted that hydroelastic effects are only relevant for small relative angles between the body surface and the fluid. He also defined a “slamming parameter” by relating the characteristic wetting time – or the duration of the hydrodynamic load – of the rigid wedge to the natural period of the shell plating stiffeners. He drew conclusions about the influence of hydroelasticity for certain ranges of the slamming parameter and mentioned that the primary variables determining a vessel's response to slamming are impact velocity and deadrise angle. In his final remarks, though, he mentioned that lower maximum stresses were observed than predicted by his quasi-steady theory for cases where the hydroelastic effects were significant.

Savander et al [15] presents extensions to Vorus' theory [18] by generalizing the model to allow for variation of both transverse and longitudinal deadrise contours in an effort to improve the analysis of three-dimensional planing surfaces. Comparable results were obtained with a few exceptions that were justified by comparison with experimental wedge drop tests performed by Peterson et al [12] at the Naval Surface Warfare Center, Dahlgren Division. Added mass, acceleration, lift, and pressure were the primary results that were presented. The model used by Peterson et al [12] was constructed from aluminum and had the following characteristics: length of 8 ft, breadth of 2 ft, and constant deadrise of 20°. Savander was concerned with the influence of hydroelasticity on the resistance characteristics of a ship and thus included some discussion of his model's predictions of lift generation at foreword and after sections of a hull.

Royce [14] extended Vorus' [18] theoretical model by including the reattachment of separated flow for two-dimensional impact. His computational model employed time integration of the kinematic boundary condition on the free contour located between the separation point and the jet head. Royce also performed full-scale experiments with a 21 ft planing ski boat to collect hydrodynamic pressure data by means of 200 through-hull fittings employing static pressure manometry. This was used for validation of his computational model. Drop test experiments with an aluminum wedge were also performed, at both the University of New Orleans and the Naval Surface Warfare Center – Coastal System Station. Tests were performed with a rigid cylinder and also with a cylinder utilizing a method for hydroelastic shock mitigation which incorporated air bag "end springs" at the chine end of the deadrise panel. This arrangement was shown to increase the hull's ability to absorb the kinetic energy present in free fall. Global vertical accelerations were measured for 3 drop heights (2 ft, 4 ft, and 6 ft), with 2 different weights (339 lbs and 711 lbs), and with two different air bag pressures (20 psi and 36 psi). A significant decrease in acceleration was seen between the rigid cylinder and the cylinder fitted with air bags.

Judge et al [9] performed drop tests with an aluminum wedge with a length of 1.509 ft, breadth of 0.656 ft, and symmetric deadrise of 37°. Cases with both horizontal and vertical impact velocities were studied. Also included were asymmetric impact tests achieved by releasing the wedge from a range of initial heel angles. A comparison study was performed to validate the results of a numerical method with the experimental results, and good agreement was found. The numerical method was designed to represent the body surface as a distribution of two-dimensional vortices.

Ikeda et al [8] presents the experimental results of 15° deadrise aluminum wedge. Specifically, the slamming pressures were measured by means of vertical drop tests. The model used in the experiments had the following principal dimensions: length of 49.21 in. and breadth of 47.24 in. Ikeda [7] presents similar results for the same wedge as Ikeda [8] on all measured data and also introduces acceleration measurements. In both papers [7, 8] discussion of the difficulties associated with high speed imaging is included. Strain and deflection calculations are mentioned and preliminary results of plate deformation are presented using a "commercially available Stereoscopic-Particle Image Velocimetry (S-PIV) software" in [8].

Panciroli [11] investigated the responses of deformable bodies experiencing slamming by means of experiments as well as computational analysis. Asymmetry of entry was included in the investigation, and rigid body dynamics and local panel strains were the topics of focus. Numerical simulation was accomplished by the results of a smooth particle hydrodynamics (SPH) model coupled with a finite element method. Similar to the present work, strain gages were the primary instruments used to capture the local structural deformations on the deadrise panels. Two strain gages were used on the panel of interest to observe the material's response at impact. The calculations made with strain gage data are similar to the present analysis, except eight strain gages were used and placed at incremental locations between the keel and hard chine in the present experiments.

1.2 Overview and Scope of Present Investigation

Analytical studies such as panel method codes and strip theory codes have produced results which indicate that the flow physics change with varying body contours, therefore it is desirable to collect time domain information about the changes in deadrise panel contour for the aluminum wedge of interest. This information is necessary to enhance the analysis of shell plating response and dynamic structural loading. It is also useful in validating UNO's in-house computational models developed by Taravella [16]. For each wedge drop experiment performed the following items are collected: pressure data, surface strain data, vertical displacement and acceleration, and high speed stereo videos of the deadrise panel surface. The pressure data is useful for obtaining loading information on the plates' exteriors, while surface strain data allows for a better understanding of the structural response. The vertical motions data permit the observation of global wedge response relative to certain time frames, especially the corresponding impact time. High speed stereo videos are analyzed to map full 3D strain fields of the panel deflection. As discussed later in chapter 3 and chapter 4, difficulty was experienced in capturing stereo videos.

The present study broadly encompasses the following: experiments used to observe the hydroelastic behavior in response to slamming impact loads and comparison with analytical models. Primarily this work is focused on the presentation and analysis of wedge drop experiment results and the development of conclusions regarding the hydroelastic effects on the accompanying flow physics. Much effort is invested in the discussion of calculating deadrise panel deflection throughout the impact events. A comparison study with Taravella [16] is incorporated to provide cross-validation. More experiments with varying wedge characteristics and drop conditions are certainly legitimate extensions that will be implemented in the future scope of this research. Further studies and testing will be executed at UNO, and the results will be appropriately analyzed and reported.

The experimental setup and drop test procedures are explained in detail in chapter 2. Numerous photographs and illustrations are provided for clarity. Further details pertaining to the setup and testing are mentioned as necessary in later sections to facilitate the descriptions of the analysis methods and results.

Chapter 3 discusses the use of *Stereoscopic-Digital Image Correlation* (S-DIC) in analyzing the deformations of a vessel's shell plating caused by slamming. DIC is a technique utilizing a high speed camera to capture the behavior of a material's surface during events which cause it to compress, elongate, or fracture. S-DIC is an extension to DIC which incorporates a second camera (or more) to reconstruct the three dimensional characteristics of the object of interest. A discussion of necessary changes in the experimental setup, the stereo cameras and the pairs of images obtained, the drop tests performed, and the methodology implemented is presented.

The results of the experiments carried out at UNO are presented and analyzed in chapter 4. Details concerning the following characteristics are discussed: hydrodynamic pressures, deadrise panel deflections, and global vertical wedge motions including position, velocity, and acceleration. The results obtained during the experiments and post-processing provide opportunities to make comparisons and conclusions.

Chapter 5 discusses the comparisons made with analytical codes written by Taravella [16], and some cross-examination is performed between the S-DIC and strain gage methods. Some conclusive and summary remarks are presented in chapter 6. Comments on the hydroelastic effects observed in the analyses of the experiments and what they mean for real ships are also provided. Several specific proposals are also made in chapter 6 regarding the possibilities for future work on the project. Some further developments and extensions are viable and easy to implement, while others will require more time and effort. The factors involved are discussed.

Chapter 2

Experimental Setup and Procedure

The present experiments used to observe and study the hydroelastic behavior of an aluminum planing hull involved the construction and testing of an aluminum wedge with 20° deadrise. In addition to the bottom panel deflections, pressure and strain distributions on the wetted side of the panel between the keel and the hard chine are observed, as well as the vertical motions of the entire wedge including displacement, velocity, and acceleration.

2.1 Setup and Assembly

The experimental wedge has a constant wedge-shaped cross section and resides in an aluminum frame while at rest. The wedge is suspended from above by means of a crane and quick release and is restrained by the housing frame which is secured to the carriage. A perspective view of the full wedge-frame assembly can be seen in Figure 2.1 showing its position and orientation above the water surface. The principal characteristics of the experimental wedge can be seen in Table 2.1, and some dimensioned drawings are shown in Figure 2.2.

Table 2.1: Main particulars of the experimental wedge

Particulars	Symbol	Value	Unit
Length	L	57.086	in
Breadth	B	47.244	in
Overall depth	D	21.000	in
Panel thickness	t	0.25	in
Deadrise angle	β	20.00	degrees
Weight	Δ	412.00	lb
Material	–	5086-H116	–

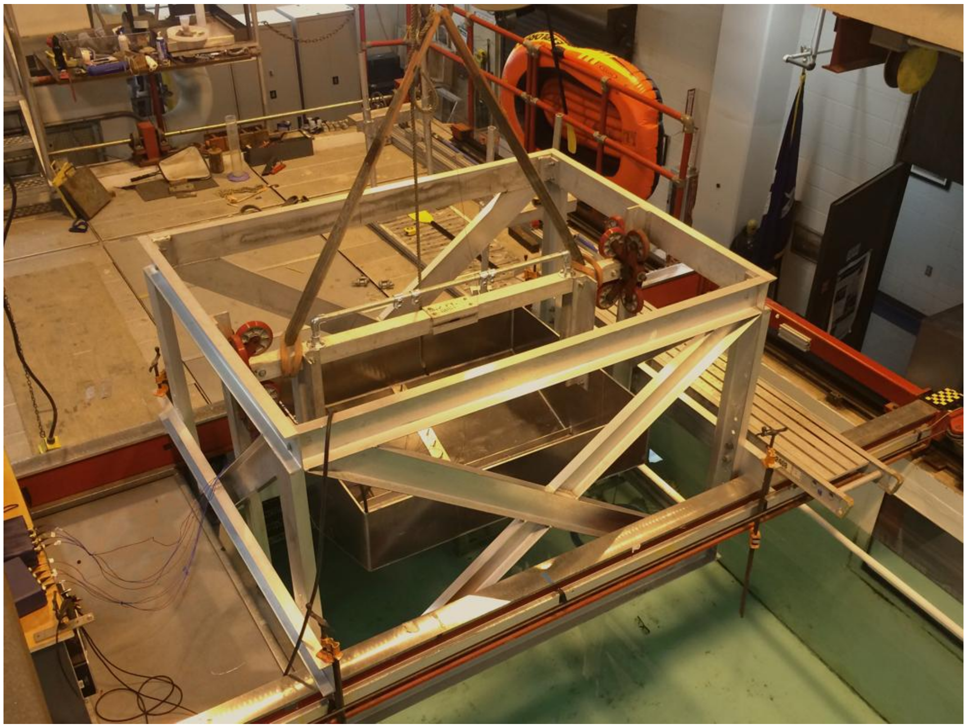

Figure 2.1: Full experimental system

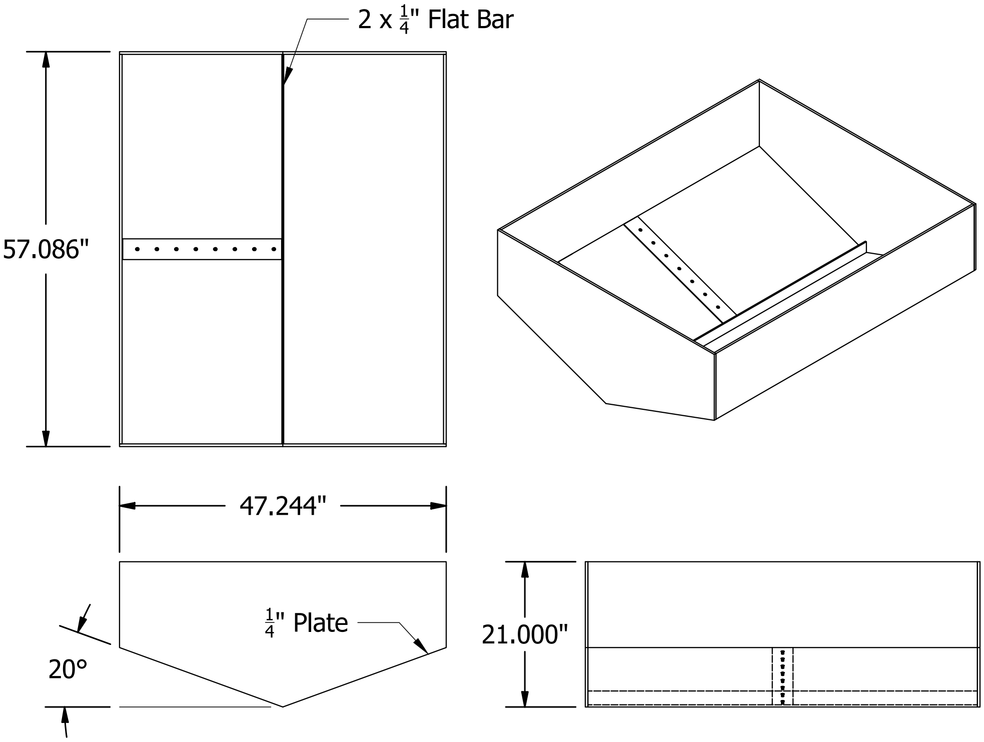

Figure 2.2: Experimental wedge

It is crucial that each drop be identical in order to study the experiment's repeatability, therefore extra care was taken in every step of construction to reduce the possibility of variation in the wedge's descent and orientation at impact. The housing frame includes rails providing for consistently vertical descents, ideally absent of deviations in the form of rotation or translation. Elevator wheels were mounted to the wedge and act as directional guides. They are hinged and pressed firmly against the vertical rails in order to provide a smooth and straight fall. The wedge is dropped by means of a quick release activated by a pull on a cable tied to the release arm. Incorporation of the quick release allows for minimized disturbance in the wedge's descent and it facilitates the operator's timing in causing the release to coincide with the data acquisition trigger. Both the quick release and the elevator wheels (on one end of the model) can be seen in Figure 2.3.

2.2 Data Acquisition

The relevant data rapidly collected during each drop test was acquired at the computer station located on the towing carriage and just outside the bottom-left corner of Figure 2.1. This is where data from the potentiometer (1 ct), accelerometers (2 ct), through-hull pressure transducers (8 ct), strain gages (8 ct), and high speed cameras (2 ct) is collected and stored. Table 2.2 gives the sample rates used in collecting time domain data for each component.

The time domain analyses studied in [4, 15, 17, 18] (and others) use a few particular instances in time as reference for their calculations. For example, analysis typically begins at

Table 2.2: Sample rates used for experiments

Component	Sample Rate
potentiometer	100,000 Hz
accelerometers	100,000 Hz
pressure transducers	100,000 Hz
strain gages	25,000 Hz
high speed cameras	varies, see chapter 3

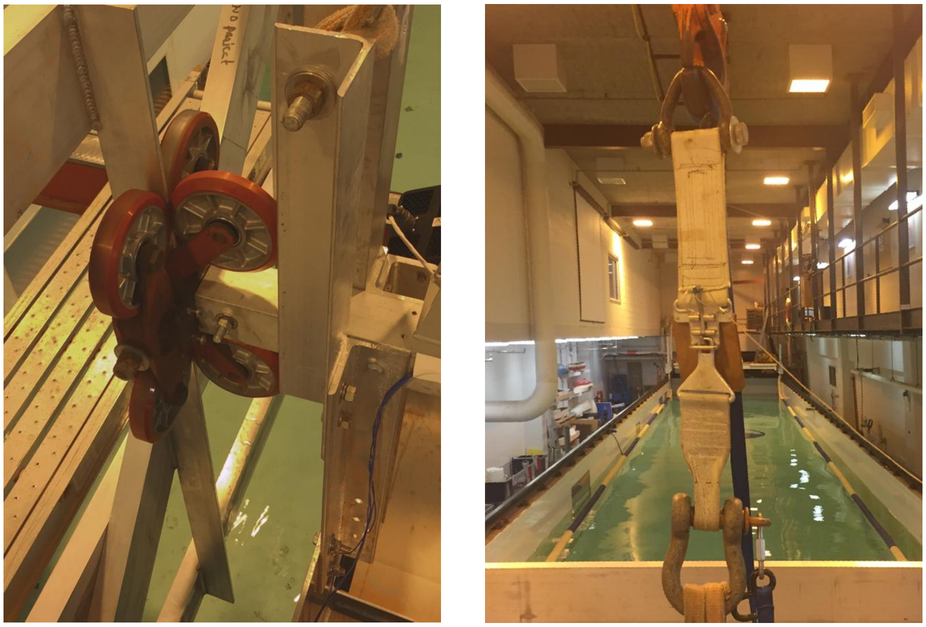

Figure 2.3: Wheels/rails assembly and quick release used to drop the wedge

impact ($t = 0 = t_0$), i.e. the moment during descent at which the bottom-most point of the wedge's keel first makes contact with the water's surface. The spatial coordinate measuring vertical position of the keel, z, is also usually considered to be equal to zero at this location (z_0). Other moments of interest are presented relative to impact, thus a negative time would correspond to a moment during free-fall, and hydrodynamic effects occur at positive times.

In order to track the vertical position of the free-falling wedge and to measure the time elapsed between moments of interest, a single string potentiometer was incorporated. It was mounted to the housing frame to reside above the wedge even at its highest point before release. A clip was set to the upper edge of the wedge's sidewall at $L/2$, half the length, and the potentiometer's string was tied to this clip so that the spool is unwound within the potentiometer causing a change in its output voltage. Figure 2.4 shows the arrangement of the potentiometer. Situating the wedge to be stable and level at $z = 0$, recording the voltage at this position, and calibrating the potentiometer to correlate a particular change in voltage with a change in linear distance of the string's displacement allows for the calculation of the wedge's vertical position at any desired time during the drop test and slamming events. The calibration factor used presently is 4 in/V.

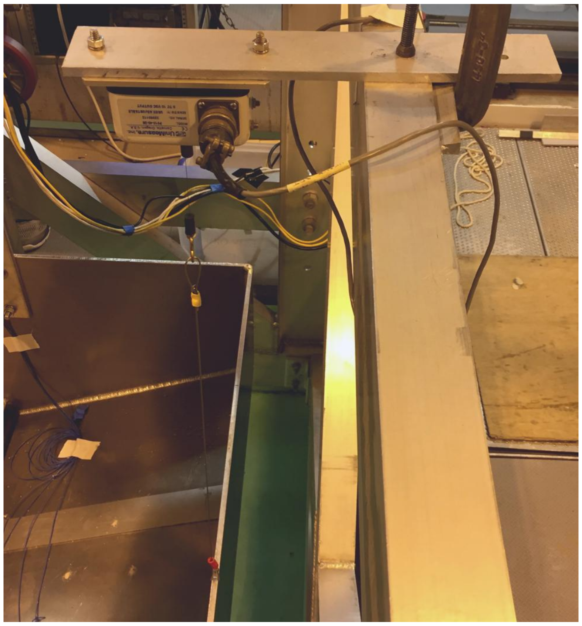

Figure 2.4: Potentiometer attachment

Two accelerometers were also incorporated in order to further examine the wedge's motions. The accelerations of the system as a rigid body or as a global system are measured and can be used to validate the time domain velocity distributions computed from the potentiometer data (changes in vertical displacement with respect to time). The accelerometers' output was used alternatively to study the behavior of the wedge at different impact velocities and also to study the relative accelerations present between various components of the system. Accelerations of two different wedge components could be analyzed for the same drop test, e.g. relative accelerations between a camera and the keel.

Data was also collected from pressure transducers and strain gages distributed along the deadrise panels from the keel to the hard chine (referred to here as a *span-wise* distribution). Both the transducers and strain gages were to be placed at $L/2$, therefore analogous span-wise locations on both sides of the wedge were utilized. Symmetry of the flows about the wedge centerline allows for comparison of this data. The pressure sensors require a particular plating thickness ($^3/_8$ in) to accurately measure hydrodynamic pressures, thus a sensor plate was included along the panel to accommodate this condition. The image on the left in Figure 2.5 is a view from above the wedge which shows the arrangement of the pressure

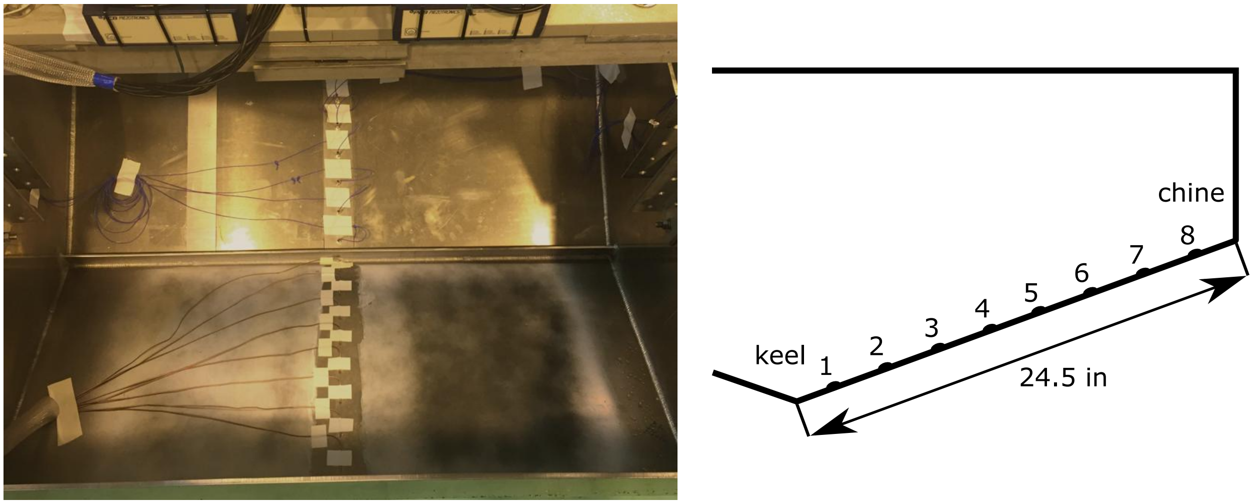

Figure 2.5: Pressure transducer and strain gage arrangements

sensors (above keel in image) and strain gages (below keel). The schematic on the right shows the numbering of the sensors and gages in increasing order from the keel to the chine. 3 inches separate each sensor, with the first starting at $1^{1}/_{4}$ inches from the keel.

A final component added to the wedge is a crossbar intended for mounting and adjusting the pair of high speed cameras and LED lights. It is necessary that the crossbar be sturdy enough to withstand the torques experienced due to the inertia of the cameras at impact. The bar should also be rigid enough to minimize any relative motions in the presence of the inevitable vibrations.

2.3 Procedure

Experimental procedures for wedge drop experiments are straightforward, but a few notes are provided for clarity. The wedge's descent is straight and vertical into calm water, so the only necessary timing to be achieved in the experiments is triggering the data acquisition systems amply before releasing the wedge from rest and collecting enough data samples to capture all interesting details, especially those occurring moments after breaching the free surface. As previously described, the present system is suspended and held at rest in the housing frame by means of a hoist crane with a D-ring shackle and two eye-eye web slings.

This arrangement can be seen in Figure 2.6. Since the shackle is situated below the quick release, it is free to fall with, and eventually into, the wedge. In order to prevent damage to the inside of the wedge, an adjustable strap was incorporated – joining the eye of the shackle's threaded pin to the crane's jaw – that catches the shackle and sling straps before they are able to crash into the wedge. This catching strap needed to be adjustable in order to accommodate various drop heights. Figure 2.3 may facilitate visualizing this arrangement, though in the image the adjustable strap passes behind the quick release.

Another procedural formality addressed prior to each drop includes ensuring that the wedge is perfectly level and parallel to the water's surface. These efforts were invested to achieve impact symmetry as best as possible. Components were also organized inside the wedge symmetrically and systematically so as to achieve a centroid located directly at $L/2$ and on centerline.

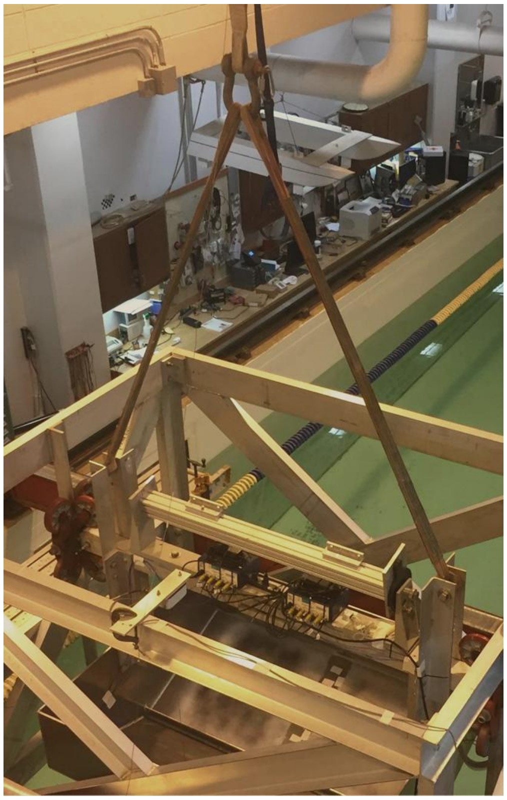

Figure 2.6: Crane and slings suspending the experimental wedge

Chapter 3

Digital Image Correlation and Image Processing

Digital image correlation is a contact-free method for measuring the surface strain and deformation experienced by a material under stress. It works by analyzing variations in a series of images taken from a fixed location and is most suitable for plat, planar surfaces. DIC has been proven to be useful in a great number of applications where tracking shifts in digital data is useful. A few examples may include scans of the human body (x-ray, CT, MRI, etc.), the optical mouse, and studying the stresses and strains in bending beams [10, 13].

Because DIC requires no physical contact, elastic deflections may be studied without hindering the expected movements of the wedge or deadrise panel. Also, other strain-capturing devices, such as extensometers and strain gages, typically observe only 1D or 2D strain fields, but stereoscopic extensions to DIC allow for the mapping of a full 3D strain field which can be used to track the displacements of surface points in any direction with respect to time. For these reasons, the development of an S-DIC code and an efficient, repeatable, and reliable method for the corresponding data acquisition produces a practical technique for studying the hydroelastic behavior of planing vessels. A simple flowchart outlining the present S-DIC algorithm can be found on page 38.

3.1 How S-DIC Works

Digital image correlation relies upon only a few main principles for operation, the first being an algorithm known as *cross-correlation* used for tracking movements in material patterns with respect to both space and time. These patterns are stored in the form of images, or more precisely, rectangular matrices of data containing information regarding the intensity of the light reflected (or emitted) by an object of interest toward the aperture of the camera(s) being used to record the patterns. As the object in the scene moves or changes shape, the reflected light will vary and the data contained in the images will be adjusted respectively.

The cross-correlation algorithm essentially checks all possible shifts of a template, or subregion, of the data from one series to the next and provides a measure, called a correlation coefficient, for each shift indicating the quality of the match. This allows for the calculation of the template's displacement in the subsequent series relative to the previous. Depending on the original image's size, the cross-correlation may be computed in the Fourier domain in order to utilize the speed and efficiency of the Fast Fourier Transform (FFT) which can provide reductions in computation time for adequately large images. The correlation is typically normalized before computing the correlation coefficients so that they are returned as scalars in the range from -1.0 to 1.0. A coefficient of -1.0 represents a match that is not at all similar to the template, while 1.0 represents an exact match. Typical values for *good* matches that are not exact (but provide confidence in correct matches) are 0.950 to 0.999.

Tracking movements of data in images using cross-correlation typically results in considerably accurate measurements. However, at least two stipulations are included: (1) the template being tracked and the original image should be scaled to identical resolutions, and (2) the template should appear in the original image exactly one time. The first requires no effort to achieve, but the second imposes the requirement that whatever pattern is applied to the tracked surface is random in nature. Therefore a random speckle pattern is typically painted on the surface of the deforming material because subsets of the pattern are easy to distinguish mathematically. Two randomly chosen templates of an image of the speckle pattern are never exactly alike. A visual example of how normalized cross-correlation (utilizing the FFT) works is provided in Figure 3.1.

Reconstruction of three-dimensional geometry is the second major step incorporated by S-DIC and is usually accomplished by means of a photogrammetric location method known as *triangulation* [2]. The task involves converting pixel coordinate measurements

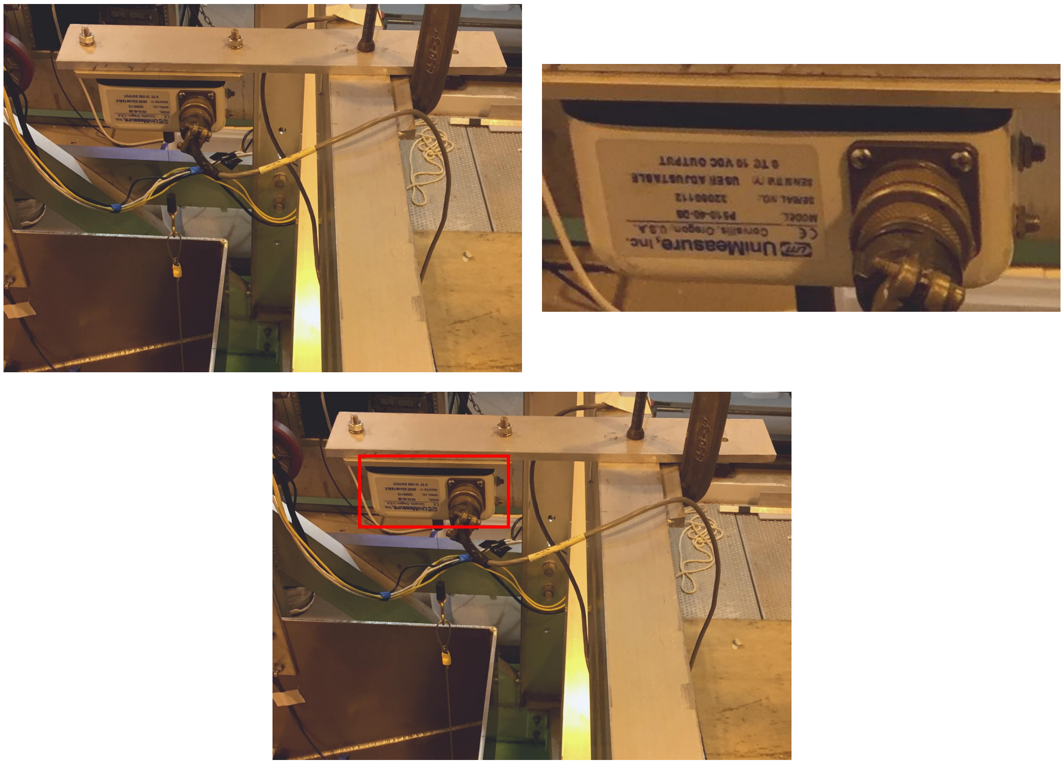

Figure 3.1: Cross-correlation example
The top-right (magnified) image of the potentiometer is the template to be found in the original image (top-left). The match is identified using cross-correlation and outlined as shown (bottom).

obtained from stereo pairs of images into spatial measurements relative to a fixed location in world dimensions. Figure 3.2 is an illustration of the geometry involved in triangulation [5]. When two cameras, at known relative locations, are capturing images of the same point, the optical center of each camera projects onto unique points, called *epipoles*, in each others' image plane. If the point of interest moves exactly along the left camera's *epipolar line*, then the point will appear to be stationary in the right camera's image plane. The same is true for the right camera's epipolar line. These two epipolar lines form the intersection between their respective image planes and the *epipolar plane*, thus they are always coplanar with the epipolar plane. An epipolar plane can be determined for any location of the point, provided that it remains in the image plane of both cameras [2].

The triangular shape of the epipolar plane gives meaning to the method's name *triangulation* and makes it possible to compute the point's distance from a reference location. These

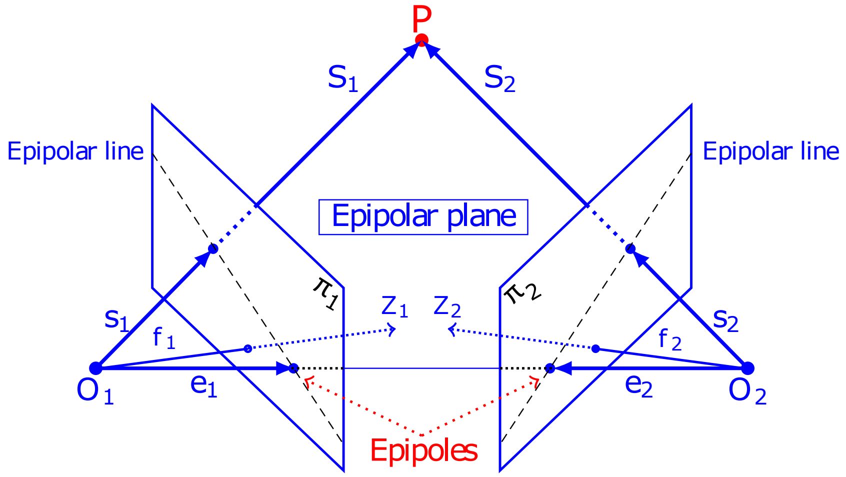

Figure 3.2: Epipolar geometry for triangulation [5]

calculations necessitate calibration of the stereo pair of cameras which includes knowledge of the position and orientation of the cameras in world coordinates, the focal length of each camera, and the location of the optical center of each camera. The origin is typically chosen to be the optical center of the left camera, therefore all computed measurements of distance and angle are given relative to this. One presently necessary assumption made in the post-processing analyses is that the cameras return to the same position despite the inevitable vibratory movements occurring in every drop. A thorough discussion of this assumption is presented in section 3.2.

Due to the concavity present in all camera lenses, any image will contain some measure of distortion, and the pixel coordinates do not exactly describe the locations of real points. Thus correcting an image for lens distortion is necessary before performing triangulation calculations and is done using each respective camera's parameters obtained by calibration.

Stereo camera calibration is performed by printing a 5×8 checkerboard (like the one shown in Figure 3.5) onto a rigid material and capturing images of it at various orientations. The pixel distances between each corner at each orientation provide information that is used to compute the camera properties. Movements of real world points at different distances away from the cameras (perpendicular to the image planes) need to be determined for S-DIC.

3.2 Experiments and Difficulties

A number of steps were taken before settling with a satisfactory methodology for DIC. The advancements made to arrive at the final implementation are presented as close to their chronological order as possible.

The chief difficulty encountered with the use of DIC in the present investigation involves the occurrence of vibratory, relative motions between the cameras and wedge. Two direct results of this vibration include the appearance of *motion blur* in the individual frames of interest and *global displacement* in images at impact relative to frames captured during calm moments. Some "bandages" can be applied to alleviate the adverse effects of this blurring and global motion, and some of the techniques used are discussed herein. Another, less severe, consequence is the necessity to assume, as previously mentioned in section 3.1, that the cameras return to their original, calm position even after having sustained a slamming event. This assumption, though, is not completely invalid, since comparisons of still images captured between drops indicate that the cameras do consistently return to the same position. Another admitted impediment was the author's initial lack of experience with high speed cameras and digital image capturing. Actions were taken to improve the overall quality of the captured videos, but the lack of expertise proved a significant drawback in the beginning.

After acquiring the experimental aluminum wedge, the inside surface of one deadrise panel was painted with a random speckle pattern which was tracked during slamming events by a stereo pair of Phantom v641 high speed cameras. An S-DIC algorithm was to be employed for the calculation of the panel's strain and deflection. The first part of this agenda was accomplished successfully, and drop tests were performed to gather data during impact for testing the S-DIC codes. However, the two primary, aforementioned hindrances were discovered at this time. Capturing images of quality high enough to be processed and used in the S-DIC algorithm proved to be challenging with the current equipment and arrangement.

Figure 3.3 illustrates the difference between an image captured during a calm moment and an image captured during a slamming event at a frame rate of 400 fps (frames per second). Even with the incorporation of motion deblurring filters, the cross-correlation routines were not able to sufficiently track the movements of any speckles as all details of the individual speckles have been lost in the blur. Useful displacement data was not obtained with the speckle pattern painted on the deadrise panel surface. These difficulties led to the eventual decision to temporarily forsake the speckle pattern in favor of painting a checkerboard pattern in its place. The painted panel can be seen in Figure 3.4. This pattern is easily processed since corner-detection algorithms are readily-available and well-developed. It also facilitates the calibration of the stereo pair of cameras when the pattern to be tracked is identical to the pattern used in calibration.

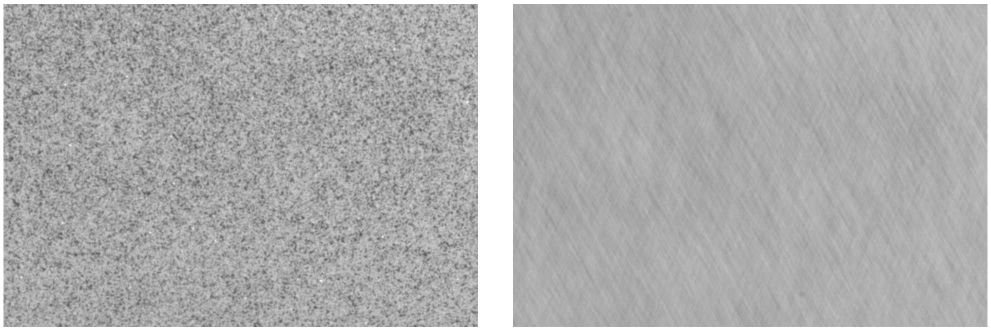

Figure 3.3: Speckle images

The square edges in the painted pattern, however, were not satisfactorily straight and clean to permit testing. So the decision was made to print the checkerboard pattern on a sheet of vellum and adhere it to the deadrise panel surface using a thin layer of Mod Podge's matte water-based glue. Some minor variations in thickness should exist due to the incorporation of the glue, but these are presently considered negligible compared to the variations present in the painted pattern. The printed panel can be seen in Figure 3.4.

Much experience was gained in using high speed cameras through the extensive efforts invested in obtaining an arrangement suitable for capturing high quality video and a usable checkerboard pattern on the deadrise panel. Numerous additional measures were taken

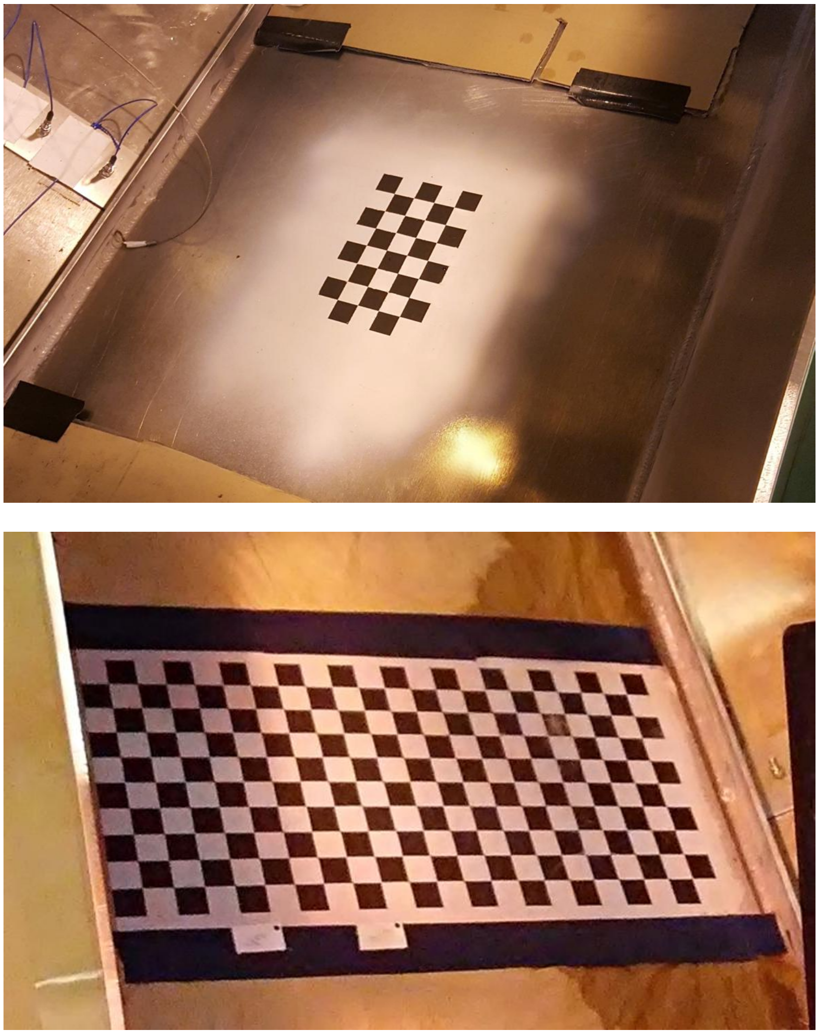

Figure 3.4: Wedge bottom with painted (top) and printed (bottom) checkerboards

to abate the unfavorable consequences of mounting cameras on a structure experiencing high impact slamming events. Further actions were taken to reduce the relative motions of the cameras: the positions of the two LED lights were adjusted in order to better suit the capturing angle of the cameras, and different frame rates were tested to reduce the troublesome effects of motion blurring. Additionally, since the vellum did not cover the entire deadrise panel, brown paper was used to cover the polished aluminum to prevent excessive light reflection. Smaller lenses (85 mm rather than 105 mm) were also incorporated allowing for a larger viewing area and better lighting. These efforts were invested to improve the overall exposure of the scene, thus enabling the frame rate to be increased from 400 to 1,400 fps. Tests incorporating speckle patterns have not yet been performed since transitioning to a checkerboard pattern, but this is a possibility for future experiments.

3.3 Image Processing and Preparation

It is desirable to collect displacement data for the entire deadrise panel surface in order to throughly study the hydroelastic response of the wedge. Time and equipment constraints prevented this complete analysis, but with just three overlapping viewing areas data was collected for an eight inch wide view covering half of the deadrise panel span. To best suit the angle of each camera relative to the deadrise panel, displacements were observed from the hard chine to the panel's midspan. The size of a camera's output viewing area is a function of the camera's position relative to the image plane and the characteristics of the lenses used. With the current arrangement, a 5 rows × 8 columns checkerboard pattern was used with 1 inch × 1 inch squares, starting with a checker in the upper-left-hand corner of the pattern. The bottom row for one view becomes the top row for the next view, thus fulfilling the overlap requirement. Figure 3.5 is a sample of the checkerboard pattern (scaled down for space preservation) which was printed and used in processing.

The acquired images must first be adequately prepared before implementing the correlation routines. This involves adjusting adverse effects such as intensity gradients, shadows, and blurring. Some of the methodology described in following was developed while processing

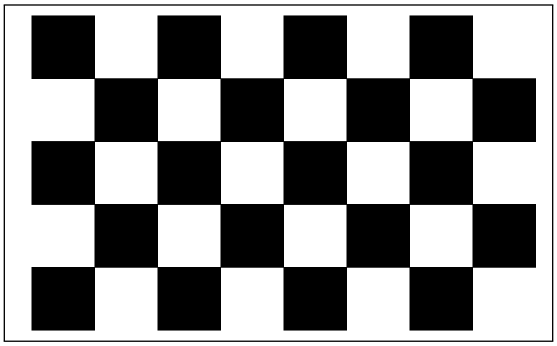

Figure 3.5: 5×8 checkerboard used in correlation (Scaled down and border added for clarity)

data gathered during experiments performed before rearrangements were made improving the overall camera exposure as discussed in section 3.2. Valuable experience was gained eliminating the necessity of performing all of these methods for every image. Nonetheless, any combination of these methods may be used in image processing before performing the S-DIC calculations.

One difficulty experienced with increasing the frame rate of a high speed camera is the loss of exposure time. Since the shutter is forced to open and close more quickly, the amount of open time that the shutter experiences decreases, allowing less light to reach the sensor. Darker images with decreased contrast between differing intensity values is a consequence of this difficulty and can be seen in a sample image shown in Figure 3.6 that will be used here for testing. To remedy these effects, the image is first sharpened to localize the gradients appearing at the square edges. The image is also cropped to remove the unnecessary paper edges on the upper-left and lower-right corners of the image. Next, the contrast of the original image is increased to intensify the difference between the black squares and the white background. The results are shown in the top left image of Figure 3.7.

However, a new issue is now more noticeable: the bottom region of the image is slightly darker than the top. This is due to the angle of the light's reflection toward the camera lenses.

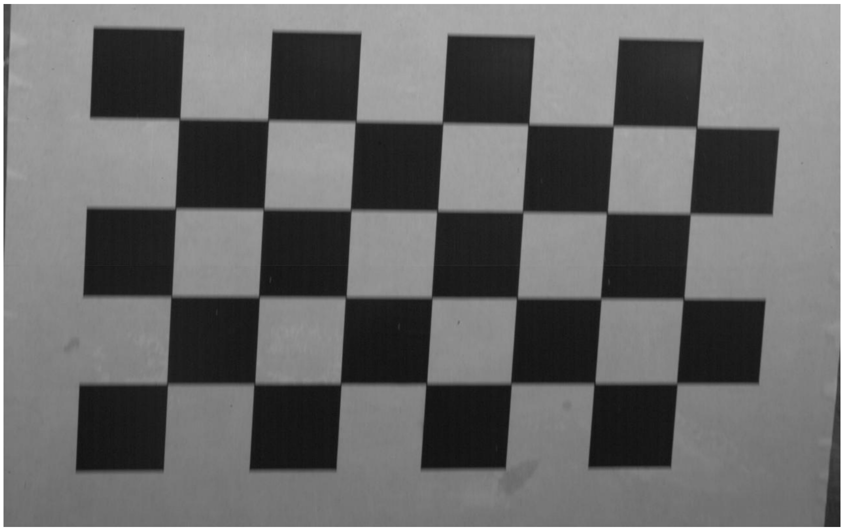

Figure 3.6: Sample unprocessed checkerboard image

A method for equalizing the overall shading of an image is implemented and is known as the *top-hat transformation* [1]. Typically, the top-hat transform involves the subtraction of the morphological *opening* of an image from the original, but a variant called the *black top-hat transform* is also commonly used which is the subtraction of the morphological *closing* of an image from the original. The present implementation is not quite either; rather, the image is first morphologically closed by a large disk-shaped structuring element of size 300. The resulting closed image is then complemented to obtain an inversion, and finally this complemented, closed image is smoothed with a Gaussian filter and added to the light areas of the original image to highlight the shadows present near the lower edge. Figure 3.7 shows the sharpened and adjusted image (TL), the morphologically closed image (TR), the smoothed complement of the closed image (BL), and the final top-hat transformation (BR). The top right image of Figure 3.7 illustrates the undesirable shadows appearing near the lower edge.

It is necessary that the structuring element for the morphological closing operation be sufficiently large to fully smooth out the gradients that would be present in the closed image due to the black/white interfaces appearing at square edges. Some square-like remains of the gradients are still evident in the top right image of Figure 3.7 despite the use of a reasonably large structuring element (this is the reason for smoothing the complemented image with a Gaussian filter). Examination of the final top-hat transformation image (bottom right of Figure 3.7) illustrates the effectiveness of the current method in preparing dark, low-contrast images with shadows for checkerboard corner detection.

Depending on the frame rate used during the drop test of interest and the amplitude of the shakes experienced by the cameras, some blurring effects may be present that may cause the corner detection algorithm to either fail or place the corner coordinates at erroneous locations. The present test image contains a significant amount of motion blur that can be seen with greater clarity in Figure 3.8. It is desirable to minimize the number of pixels required to fully transition from the low intensity values defining the checkerboard squares

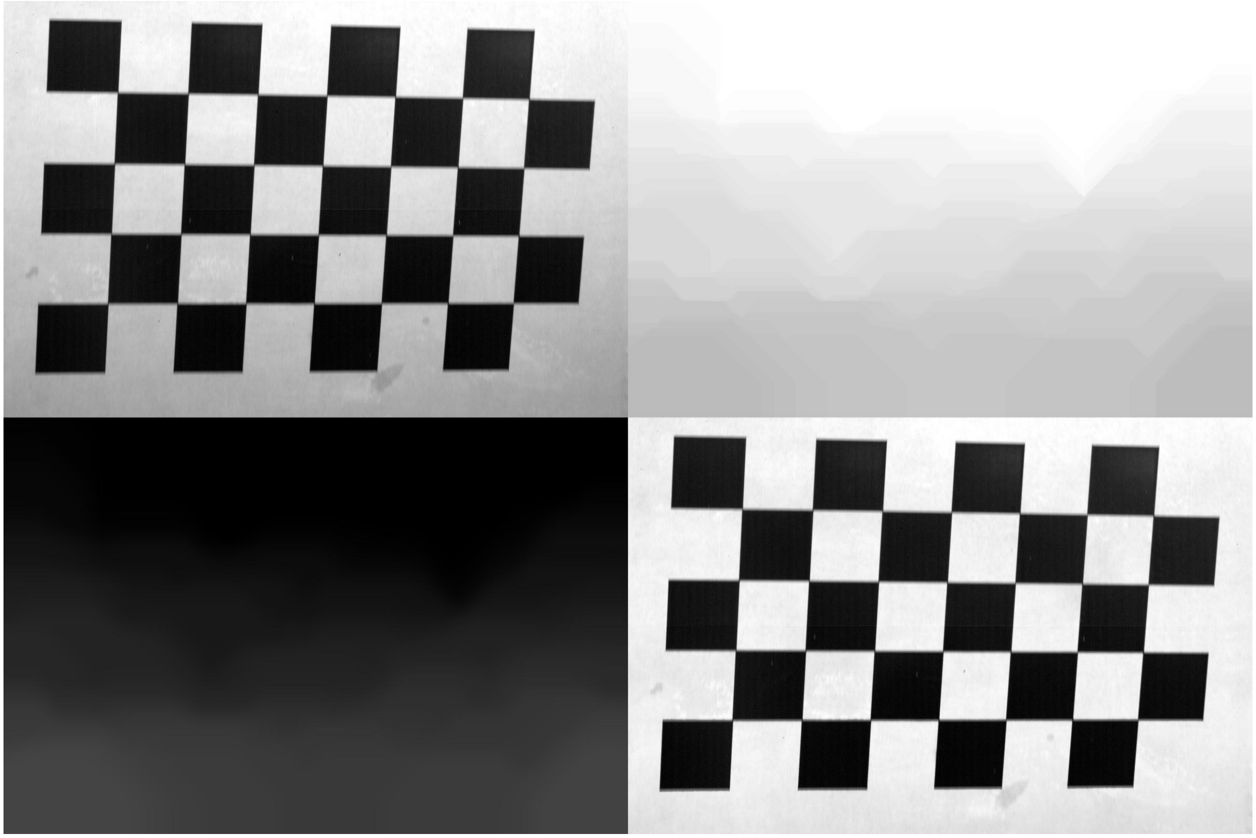

Figure 3.7: Top-hat transformation

to the high intensity values defining the paper on which the squares are printed. The square corners magnified in Figure 3.8 are separated by approximately 15 pixels indicating that the corner detection algorithm could easily place this intersection's coordinates at least 7.5 pixels away from its exact location. Thus it is necessary to investigate methods facilitating the determination of a more precise location. Numerous algorithms are available for implementing deblurring techniques, and a method known as the Lucy-Richardson (L-R) iterative deblurring algorithm is used presently to remove these troublesome motion blurring effects.

The L-R method is most frequently used for the removal of Poisson noise, which is characterized by random occurrences of light noise and is typically associated with the particle nature of light, from rasterized images [3]. Though blurring due to motion is the present difficulty, the L-R algorithm is acceptable for use in its removal as illustrated in Figure 3.9. It works by calculating a point-spread function – determined by estimating the magnitude

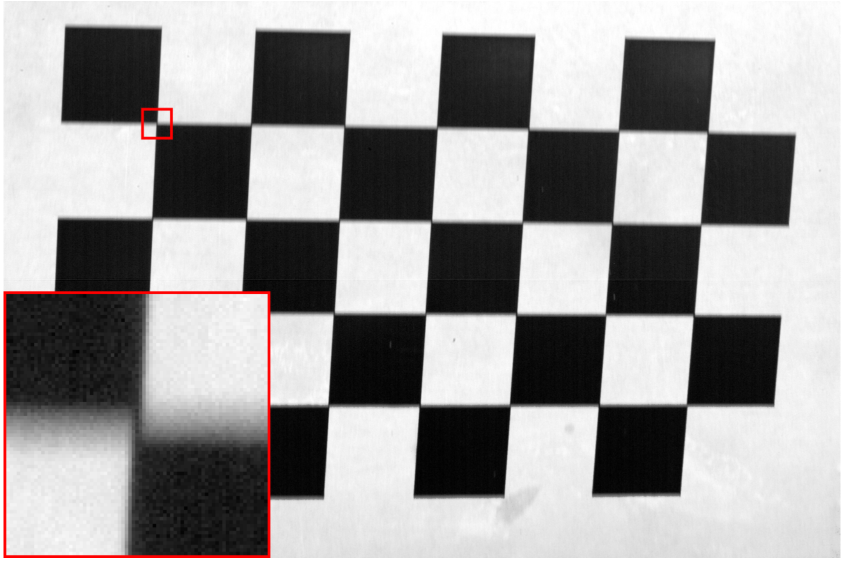

Figure 3.8: Blurring due to camera motion

and direction of the camera movement causing the blur – and using this function to perform deconvolution in the Fourier domain. Figure 3.9 shows the results after implementing the algorithm. The corner is no longer separated and the transition of low to high intensity pixels occurs over approximately 3 to 4 pixels instead of 15. The high gradients defining square edges have been almost perfectly restored. The horizontal, wave-like shadows appearing near the edges of the squares after applying the L-R method are of little concern considering the success of deblurring and can easily be removed by spectral processing – e.g. filtering in the Fourier (or frequency) domain – or even more simply by thresholding the image. Thresholding is performed regardless of using spectral methods in order to improve the speed of the corner detection algorithm, so this is the preferred alternative. After thresholding the image shown in Figure 3.9, a small Gaussian filter is applied to smooth the edges that appear in the resulting binary image and the corner detection algorithm is implemented, the results of which are illustrated in Figure 3.10. A small circle is drawn around each corner using the coordinates returned by the corner detection function to verify that the coordinates appear directly at the intersections of the squares edges. Figure 3.11 illustrates the improvements of the corner details from start to finish. Significant enhancements are evident, both in square/background contrast and in deblurring.

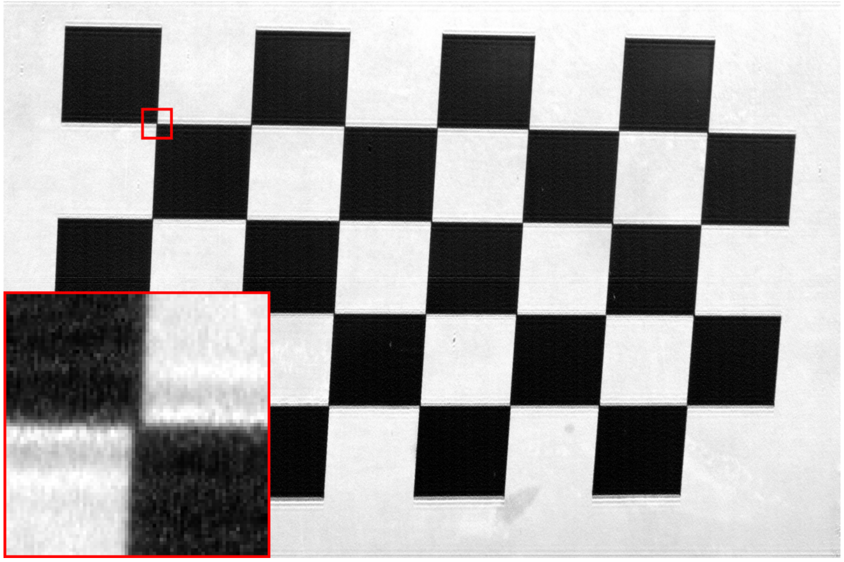

Figure 3.9: Image after deblurring with Lucy-Richardson method

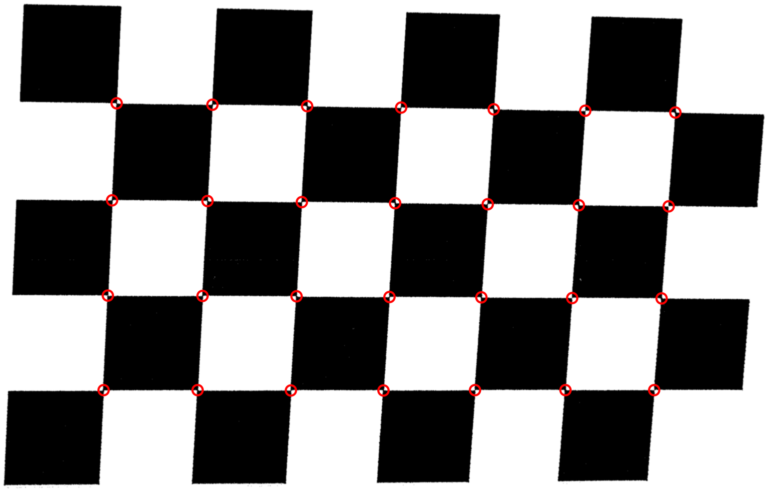

Figure 3.10: Final image after all processing; detected corners are circled

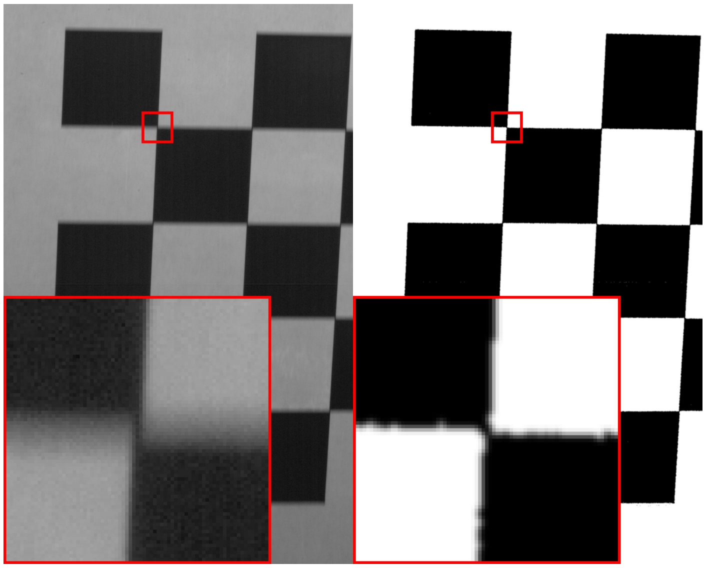

Figure 3.11: Corner detail comparison

3.3.1 Vibration Subtraction, Method 1

As discussed previously in section 3.1, the geometry involved in triangulation calculations requires that the pair of cameras remain motionless relative to the objects being captured. Thus, it is necessary that the cameras experience exactly the same motions experienced by the wedge as a global system. Therefore the cameras' connections to the wedge should be as rigid as possible. Due to the difficulties mentioned in section 3.2, relative motions were present in each test, and measures must be taken in post-processing to alleviate the problem of the shaking cameras. Two methods for dealing with this issue are described.

Method 1 involves tracking the global motions of the entire checkerboard pattern of interest. After the images have been satisfactorily prepared and improved for calculations, normalized cross-correlation between a still image (captured before the vibration) and a displaced image (captured during a slamming event) is performed. A portion of the image moves off the edge of the image boarder from one frame to the next, thus, when performing cross-correlation between frames, it is helpful to select the correlation template to be the entire image less a border around the edge. This prevents the correlation routine from returning erroneous displacements. An illustration of this description can be seen in Figure 3.13. The top shows the correlation template in the undisplaced image, and the bottom shows the location of the best match found in the displaced image.

Method 1 essentially locates the whole checkerboard pattern in a particular frame of interest and measures the horizontal and vertical movements Δx_j and Δy_j between the motionless and current frames in pixel dimensions. These shifts are subtracted from the checkerboard corner coordinates $\left(x_j, y_j\right)$ as shown in Equation 3.1. After subtracting this Δx_j and Δy_j from the corner coordinates, the algorithm has effectively lined up the checkerboard patterns found in each frame. The subscript j indicates the current view.

$$\begin{aligned} x_j &= x_j - \Delta x_j \\ y_j &= y_j - \Delta y_j \end{aligned} \tag{3.1}$$

This algorithm is quick and reliable, but issues are expected to arise in performing the triangulation calculations due to the issue illustrated in Figure 3.12. Neither of the cameras' image planes are parallel to the surface of the deadrise panel, so a component of the out-of-plane deformations experienced by the panel will be subtracted in this operation. If a point on the panel's surface does not move exactly in the direction of the camera's aperture, then the subtraction routine will inevitably subtract its translational movement when aligning the deflected pattern with the still pattern. For this reason, computed deflections should appear smaller than reality.

Nonetheless, the approximation can be implemented, and a sample test is shown in Figure 3.13. The given sample's displacement is 145.0 pixels which is more than 9% of the entire (cropped) image's height. The red circle corresponds, in both images, to the pixel coordinates of the center of the correlation template located in the original image. The blue circle indicates the pixel coordinates of the center of the matched area in the displaced image.

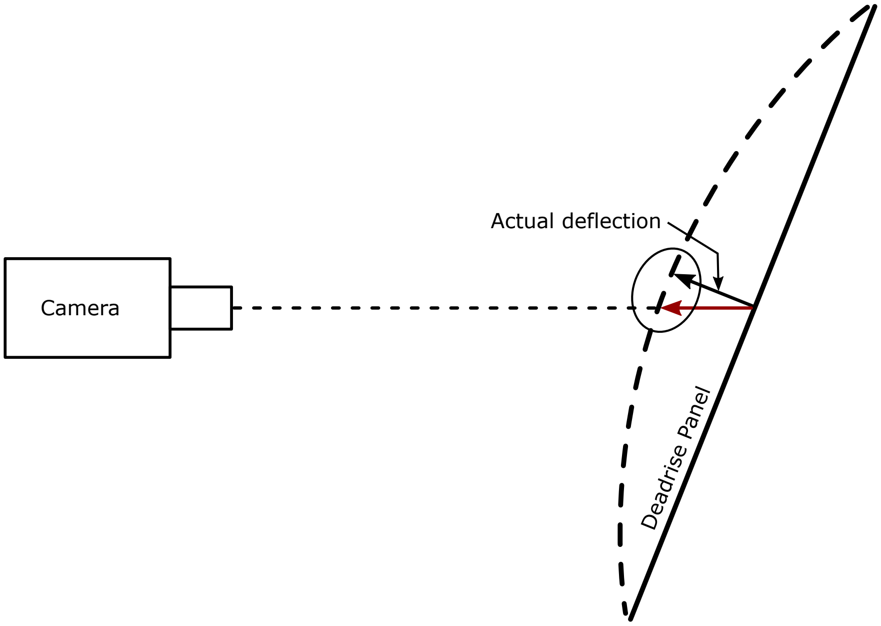

Figure 3.12: Shaky camera problem

3.3.2 Vibration Subtraction, Method 2

The following procedure was designed to improve the accuracy of the subtractions made in removing the image displacements due to camera motion from the checkerboard corner coordinates. While method 1 relies upon correlation to track the movements of the checkerboard as a whole, method 2 is based on computing the displacements of stationary markers that appear in all frames. The markers were placed at the chine weld and next to every fifth row of checker corners as shown in Figure 3.14 and Figure 3.15.

The algorithm is relatively simple, though visualizing the concept is not trivial. Starting with view 1 and the marker drawn on the chine weld, the marker is first identified as a template for correlation. Then correlation between that template and each impact frame is performed providing the coordinates for the marker in each frame. The horizontal and vertical distances traveled by the marker indicate the amount of motion that should be subtracted from the checkerboard corner coordinates for each frame of view 1. This can be thought of as a procedure which aligns the marker in each impact frame with the marker found in the motionless frame, but still allowing the rest of the checkerboard to deform freely. When

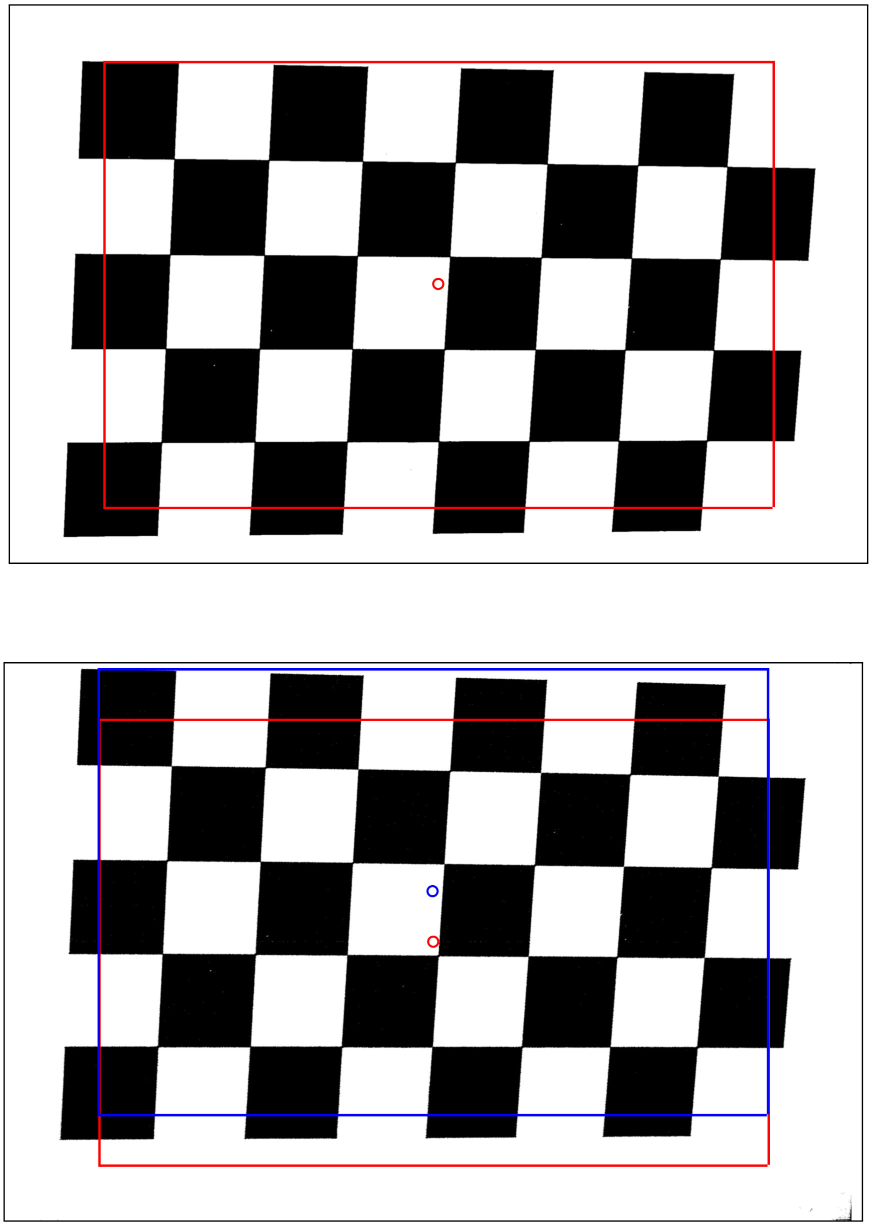

Figure 3.13: Template matching to subtract camera motions, Method 1 (The borders were added to provide clarity for the image edges)

moving on to views 2 and 3, it is necessary to subtract the horizontal and vertical distances from the previous camera views. In this manner, if all of the images from a particular time step are spliced together to form a single, large image containing all of the checkers and markers, the markers will be aligned with the chine weld held stationary. This operation can be visualized in Figure 3.16.

The following assumption is necessary to permit these calculations: corresponding frames between drops occur at exactly the same time relative to impact. In other words, for any two drop tests, corresponding post-impact frames occur at exactly the same time step. This is considered to be valid since the wedge is dropped from exactly the same height for each trial, and since the particular frame corresponding to impact can easily be determined. More discussion on this is provided in chapter 6.

The algorithm may be briefly outlined as follows. The explanation below uses the following convention: a marker displacement $\Delta x_{i,j}$ represents a movement tracked between frames for marker i and view j. It is computed by locating the marker in two adjacent views j and $j-1$ and subtracting its coordinates in view j from the coordinates in view $j-1$.

1. Locate markers 1 and 2 as correlation templates in view 1
2. Use cross-correlation to determine coordinates of markers 1 and 2 in view 1
3. Use cross-correlation to determine coordinates of marker 2 in view 2
4. Determine the following:
    - horizontal and vertical movements for marker 1 in view 1 ($\Delta x_{1,1}$,$\Delta y_{1,1}$)
    - horizontal and vertical movements for marker 2 in view 1 ($\Delta x_{2,1}$,$\Delta y_{2,1}$)
    - horizontal and vertical movements for marker 2 in view 2 ($\Delta x_{2,2}$,$\Delta y_{2,2}$)
5. Subtract $\Delta x_{1,1}$ and $\Delta y_{1,1}$ from corner coordinates in view 1
6. Subtract $\Delta x_{2,2}$ and $\Delta y_{2,2}$ from corner coordinates in view 2
7. Add $\Delta x_{2,1}$ and $\Delta y_{2,1}$ to corner coordinates in view 2

Steps 1 through 7 are repeated for all n views, but step 7 should include a summation of $\Delta x_{j,j-1}$ and $\Delta y_{j,j-1}$ from 1 to j for views $j \geq 2$. If an ordered pair $\left(x_j, y_j\right)$ represents the pixel coordinates of a checkerboard corner in view j, then the equations for the corner coordinates in view j for subsequent views ($j \geq 2$) are written as:

$$\begin{aligned} x_j &= x_j - \Delta x_{j,j} + \sum_{j=1}^{j} \Delta x_{j,j-1} \\ y_j &= y_j - \Delta y_{j,j} + \sum_{j=1}^{j} \Delta y_{j,j-1} \end{aligned} \tag{3.2}$$

And the equations for a corner in view 1 would simply be

$$\begin{aligned} x_j &= x_j - \Delta x_{j,j} \\ y_j &= y_j - \Delta y_{j,j} \end{aligned} \tag{3.3}$$

Extending this technique to an implementation utilizing more than three camera views would be easily accomplished. Future studies may incorporate more than three views if the same camera lenses and thus viewing areas remain unchanged. This would be done in order to study the panel deflections present along the entire span from chine to keel. Hopefully agreeable results will be seen when comparing the deflection predictions of the strain gages and S-DIC methods close to the keel.

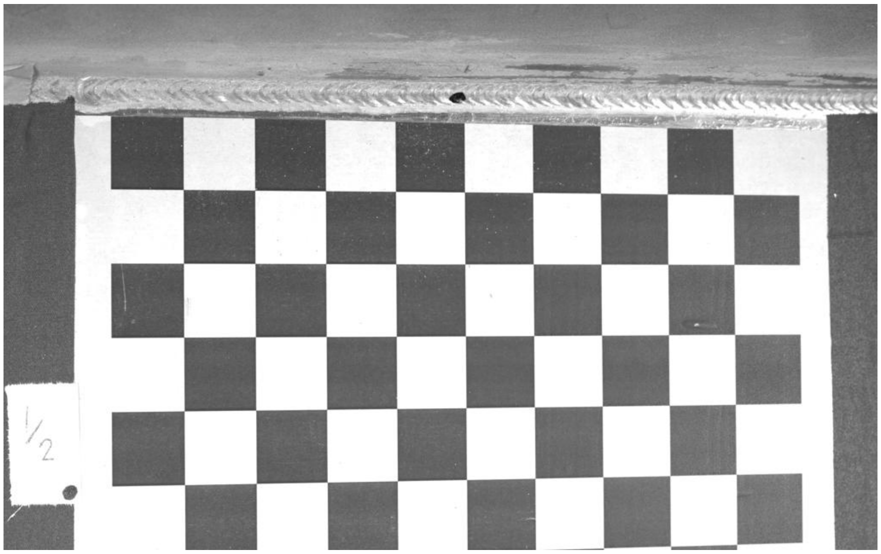

Left camera, view 1

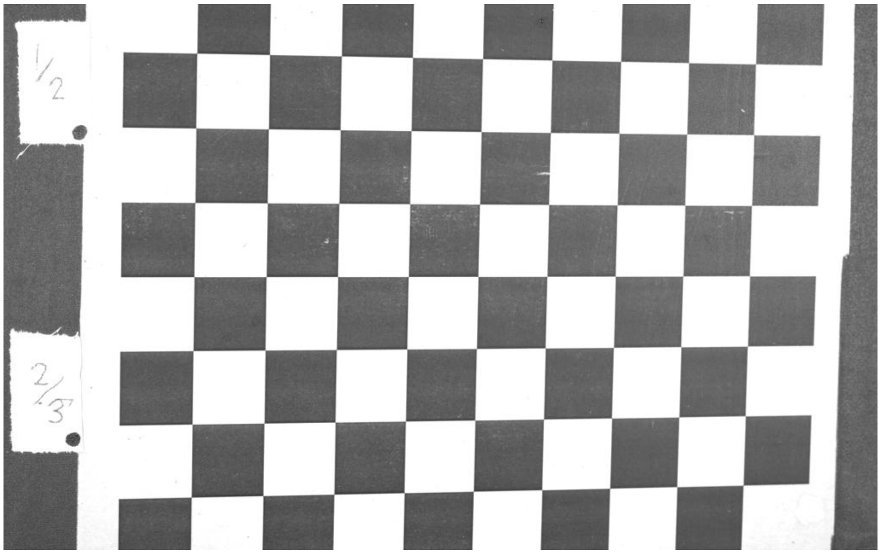

Left camera, view 2

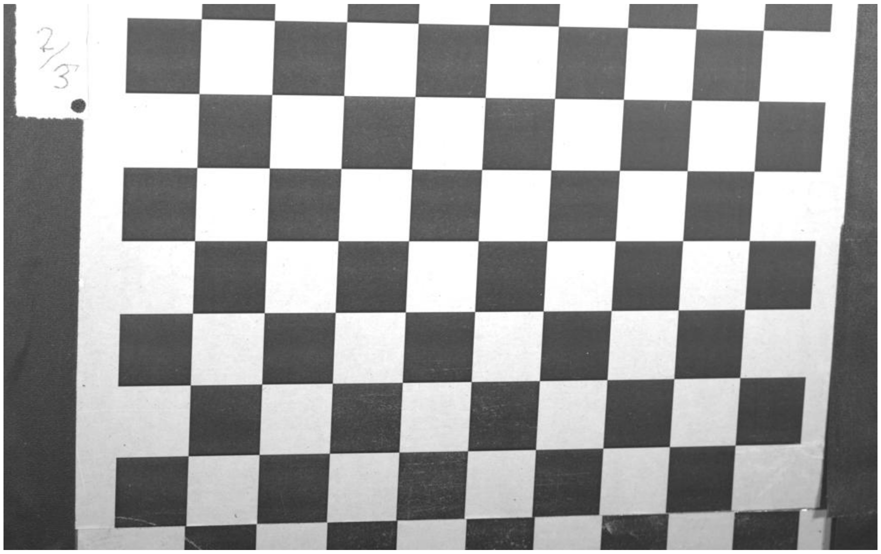

Left camera, view 3

Figure 3.14: Left camera, views 1, 2, and 3

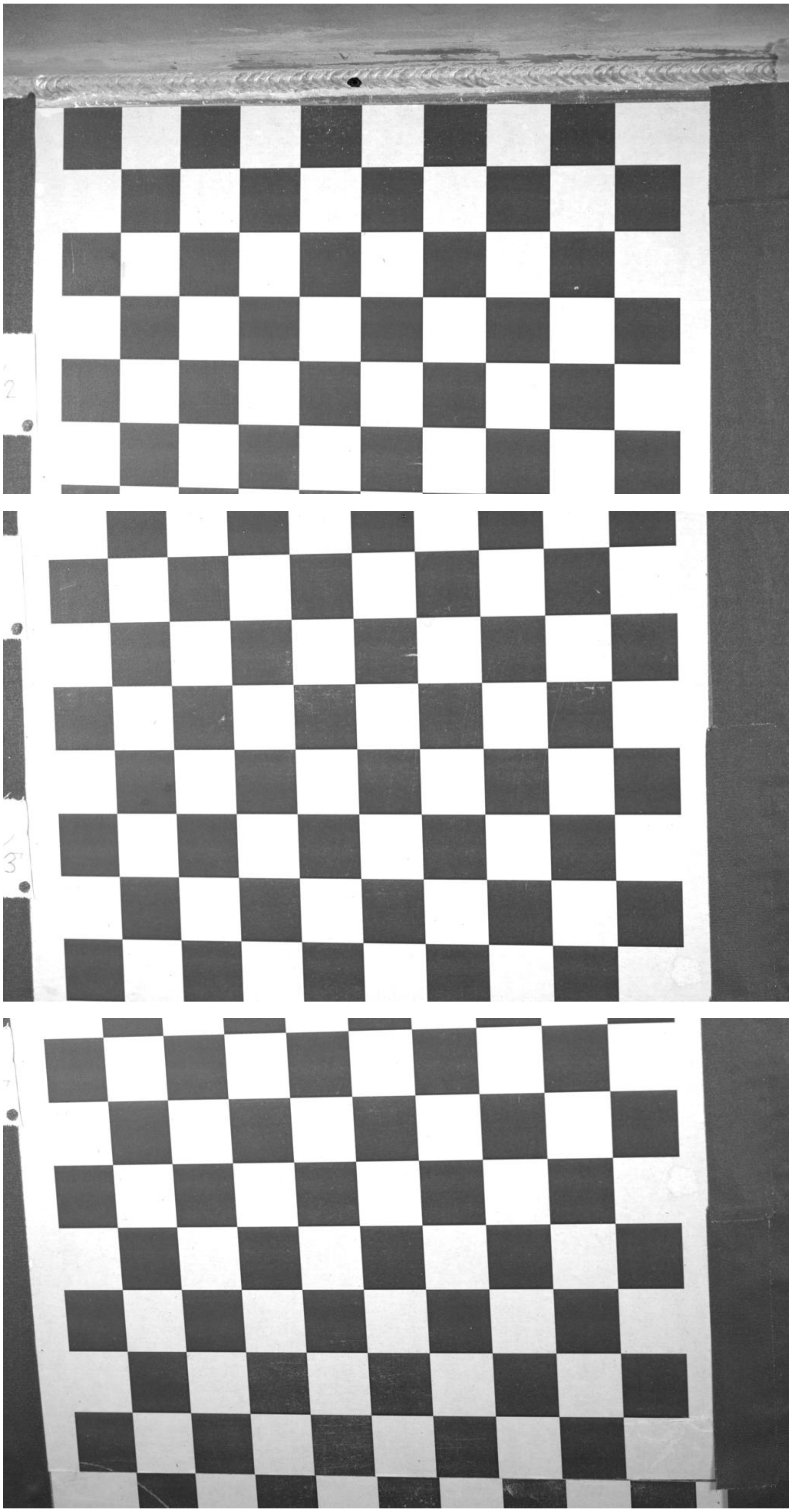

Right camera, view 1

Right camera, view 2

Right camera, view 3

Figure 3.15: Right camera, views 1, 2, and 3

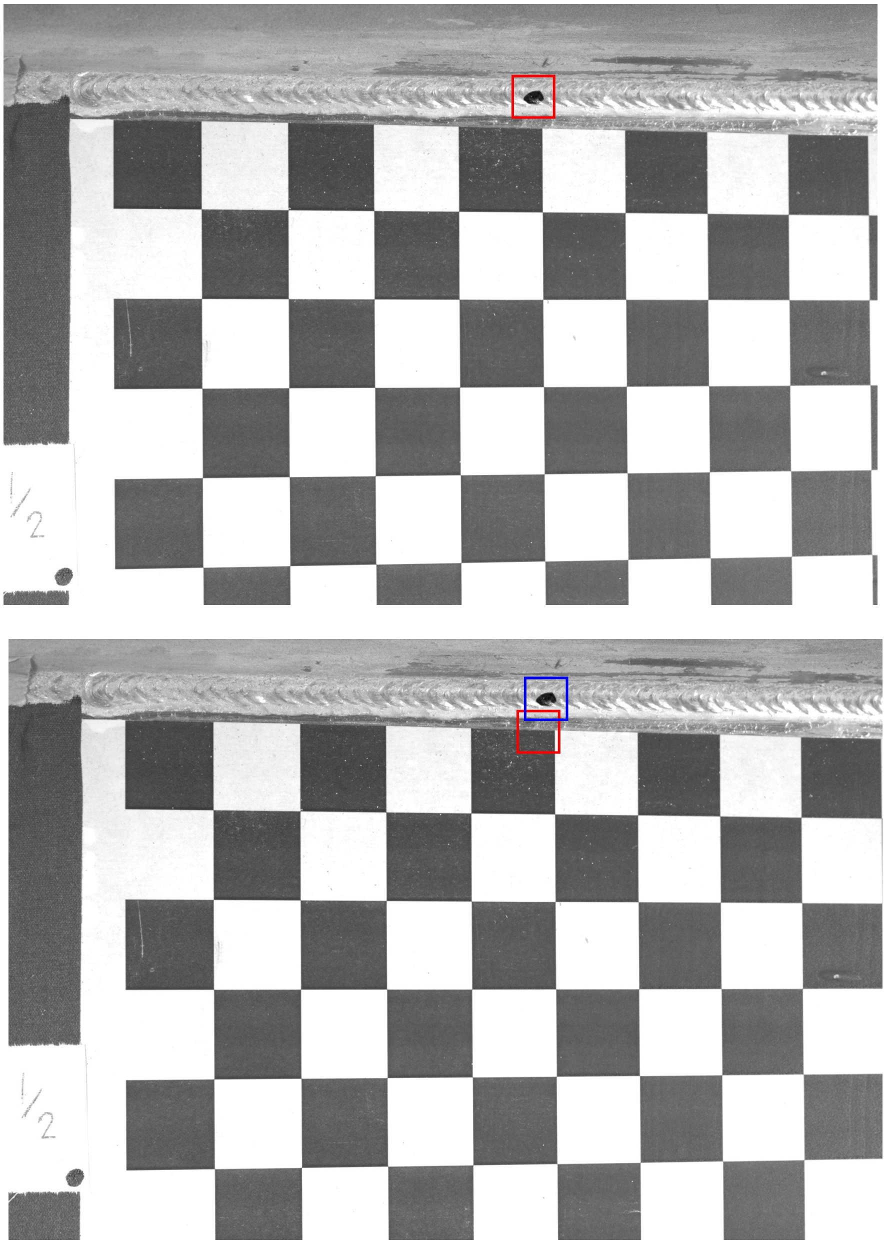

Figure 3.16: Tracking stationary markers for vibration subtraction, Method 2

S-DIC Algorithm Flowchart

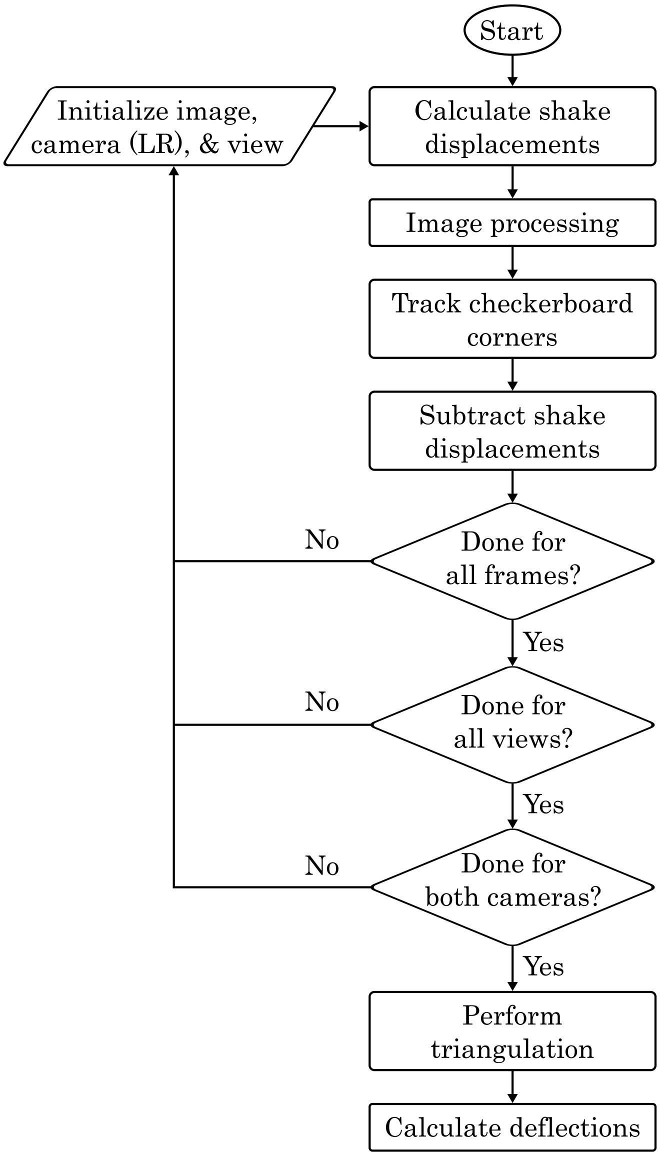

Figure 3.17: S-DIC Algorithm Flowchart

Chapter 4

Experimental Results

Numerous drop tests were performed to gather data for the analyses necessary to accomplish this thesis. Eight drop tests are emphasized in particular, so throughout the remainder of this report, *trials 1s and 2s* will refer to two unique drop tests performed in accompaniment with strain gage data collection. *Trials 1c – 6c* will refer to six unique drop tests performed with a stereo pair of high speed Phantom cameras. This convention is used to facilitate distinguishing the data in references such as plot legends, tables, and contextual discussion. As discussed in chapter 3, three camera views were required to capture panel deflections starting from the hard chine and moving down to midspan, and two drops are used at each view for comparison. Trials 1c and 2c correspond to the two drops performed to capture panel deformations near the chine, trials 3c and 4c correspond to the intermediate view, and trials 5c and 6c contain the data corresponding to panel deflections near midspan (see Figures 3.14 and 3.15). Therefore data from trials 5c and 6c are used in comparing strain gage results (trials 1s and 2s). Table 5.1 summarizes relevant data for each drop height.

4.1 Pressure

Pressure was measured on the wetted side of the deadrise panel using eight piezoelectric pressure transducers that were evenly spaced and arranged colinearly from the keel to the hard chine. The maximum pressures for trials 1s and 2s were 13.916 psi and 13.989 psi respectively, and they both occurred at 0.00121 sec after impact respectively.

Figures 4.1 – 4.4 are time domain plots of hydrodynamic pressures read by each transducer during 6 in., 12 in., 18 in., and 24 in. (trials 1s) drops respectively. The legend entries, sensors 1 through 8, correspond to the associated locations arranged from the keel to the hard chine as indicated by Figure 2.5. Interestingly, the maximum pressure measured by sensor 3 is almost equivalent to or slightly less than the highest measurement of sensor 4 in both plots. This illustrates the dynamic nature of the governing physics and the importance of the developing spray root jet discussed by Wagner, Vorus, etc. [18, 19].

4.2 Vertical Position, Velocity, and Acceleration

Figures 4.5 and 4.6 show time domain plots of position and drop speed for all drop heights of interest. Figures 4.7 and 4.8 are similar, but they show data collected in the drop tests used for capturing video for DIC analysis (trials 5c and 6c). Observation of the plots provides confidence in test repeatability and consistency. Small disparities are noticeable in impact velocity (see Table 4.1), however it should be noted that the model weight with cameras and lights is 412 lb. When testing with strain gages, the high speed cameras and its associated components were not in the wedge reducing its weight to 380 lb, a difference of about 32 lb. This alters the wedge's ability to overcome the friction in the wheels that guide its descent.

Figures 4.9 – 4.12 are plots of the global wedge acceleration measured using uniaxial accelerometers. The two accelerometers were mounted together for comparison and verification. Great sensitivity is apparent in the capturing of acceleration data.

4.3 Strain Gage Results

Table 4.1 shows maximum strains experienced by the deadrise panel measured using strain gages as well as impact velocities measured using the string potentiometer. The strain gages provide a simple, yet effective method for determining the surface strain in a single direction. Deadrise panel deflection can be computed at any time step using data collected by the strain gages. Hydroelastic panel response is this project's primary concern, therefore time domain information of the wedge's shell plating deflection is of chief importance.

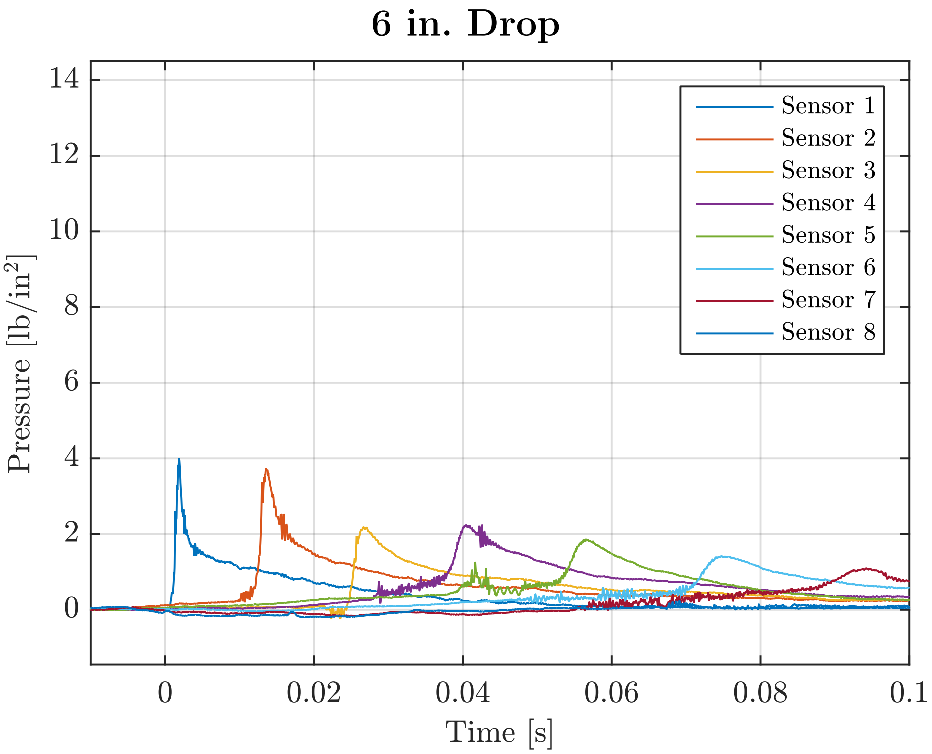

Figure 4.1: Hydrodynamic pressure, 6 in. drop

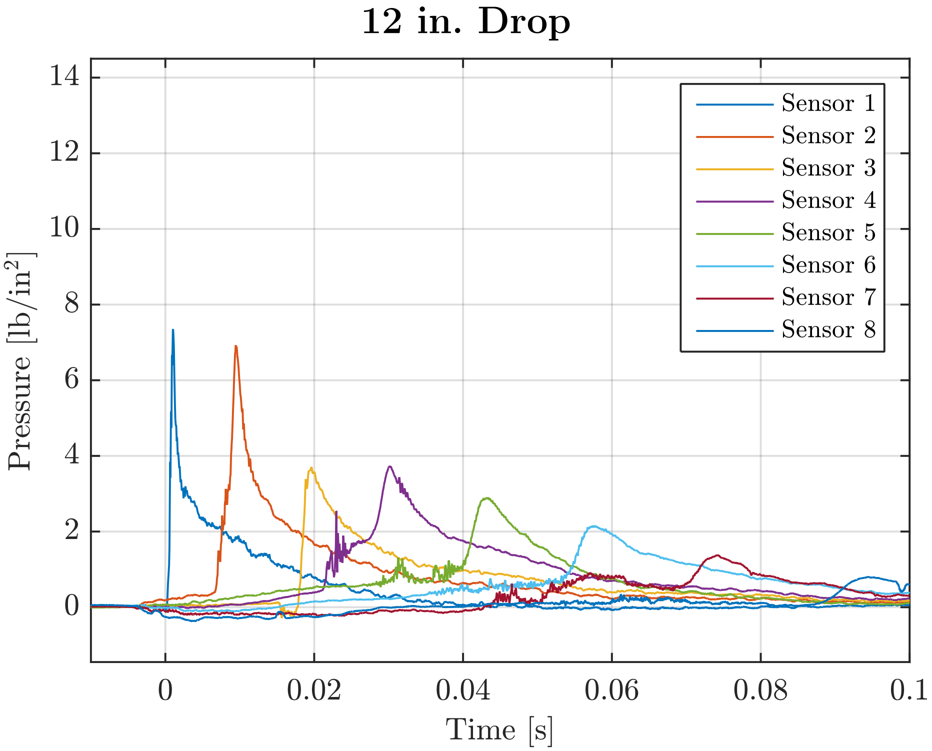

Figure 4.2: Hydrodynamic pressure, 12 in. drop

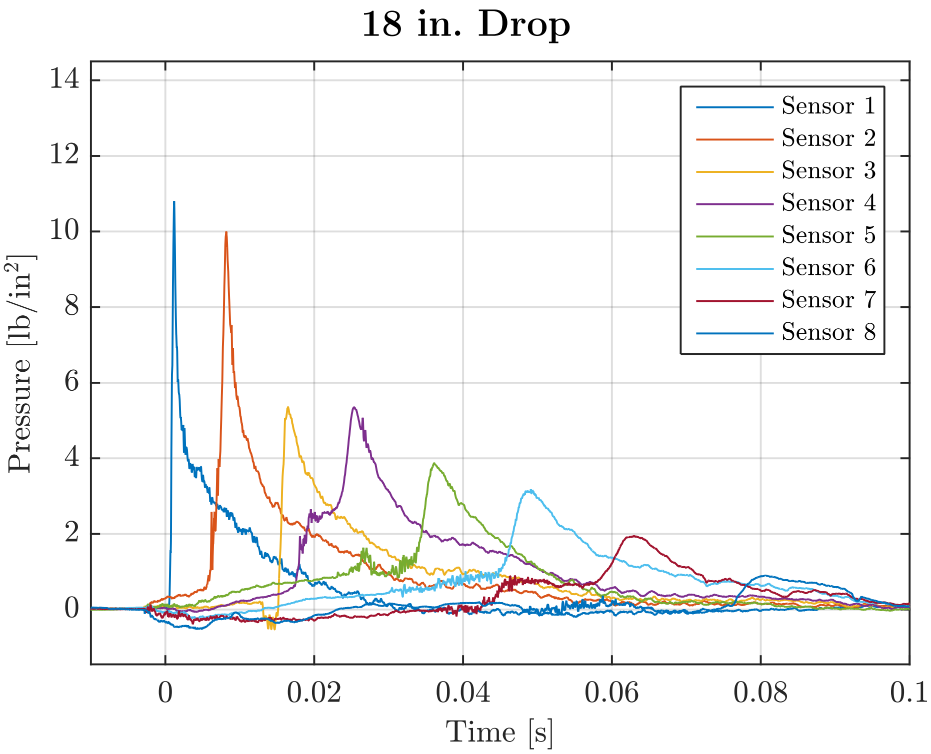

Figure 4.3: Hydrodynamic pressure, 18 in. drop

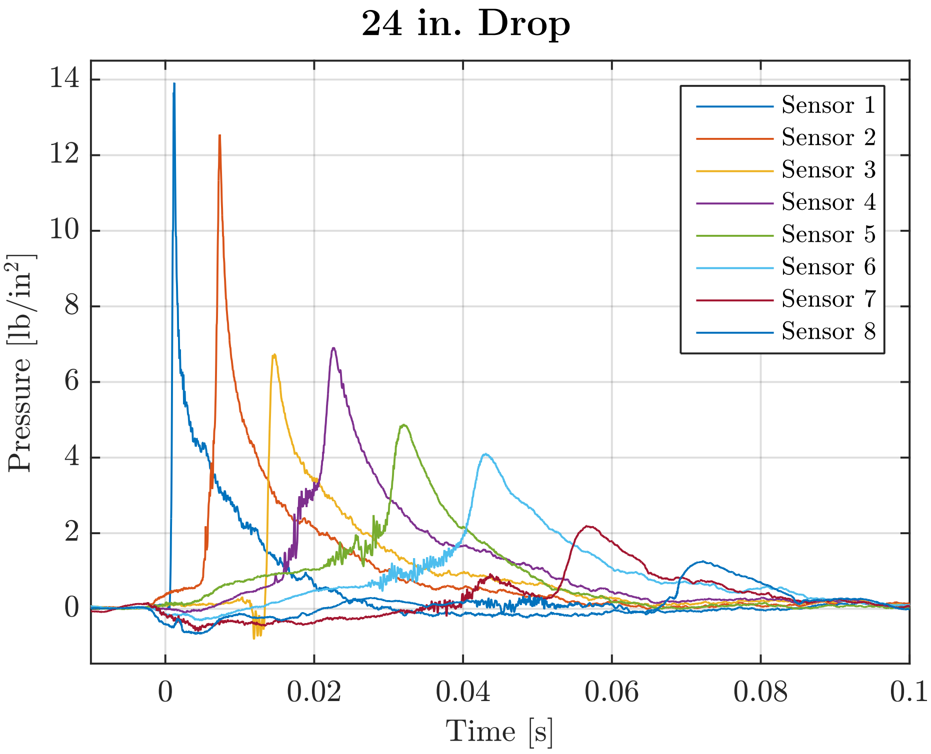

Figure 4.4: Hydrodynamic pressure, 24 in. drop (trial 1s)

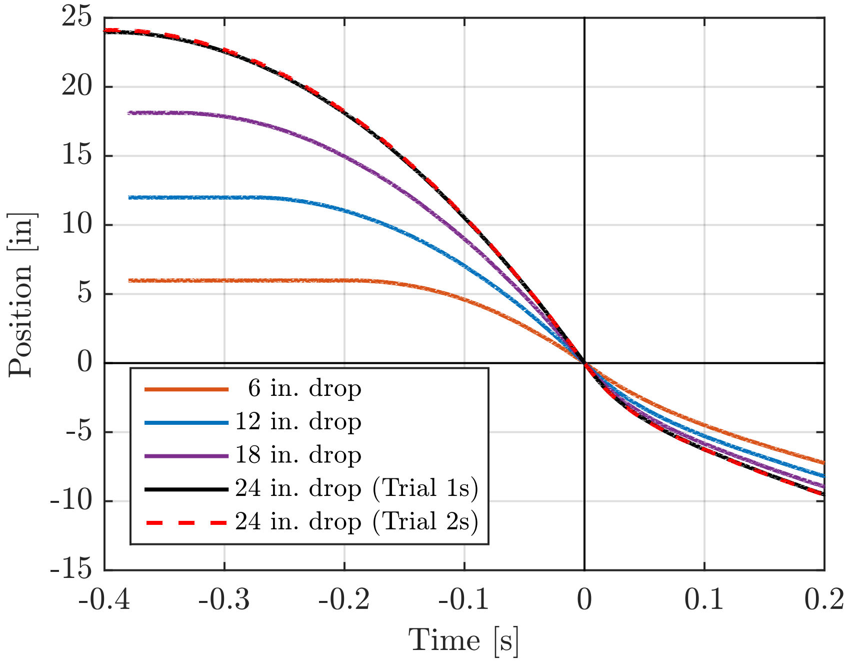

Figure 4.5: Wedge position, from drops with strain gages

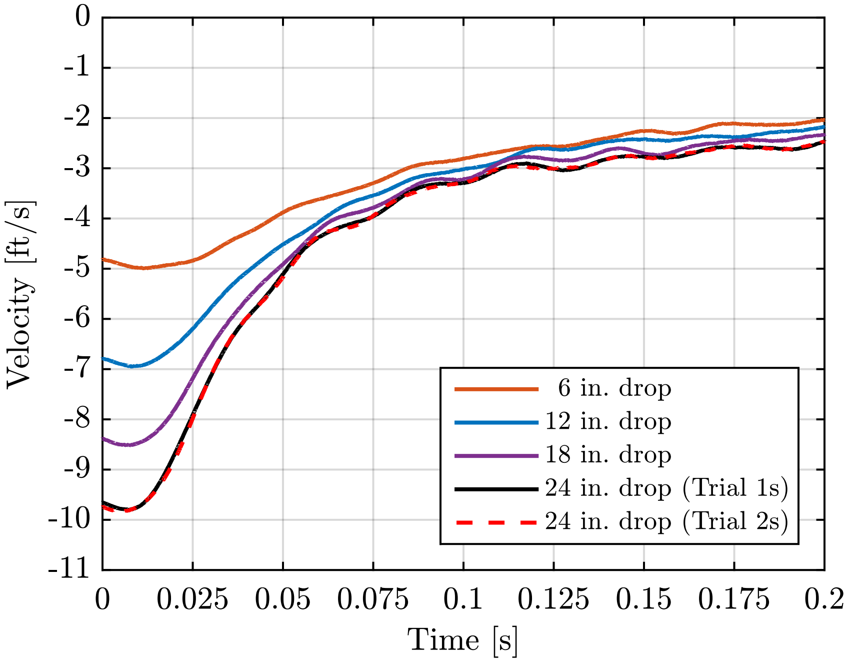

Figure 4.6: Wedge velocity, from drops with strain gages

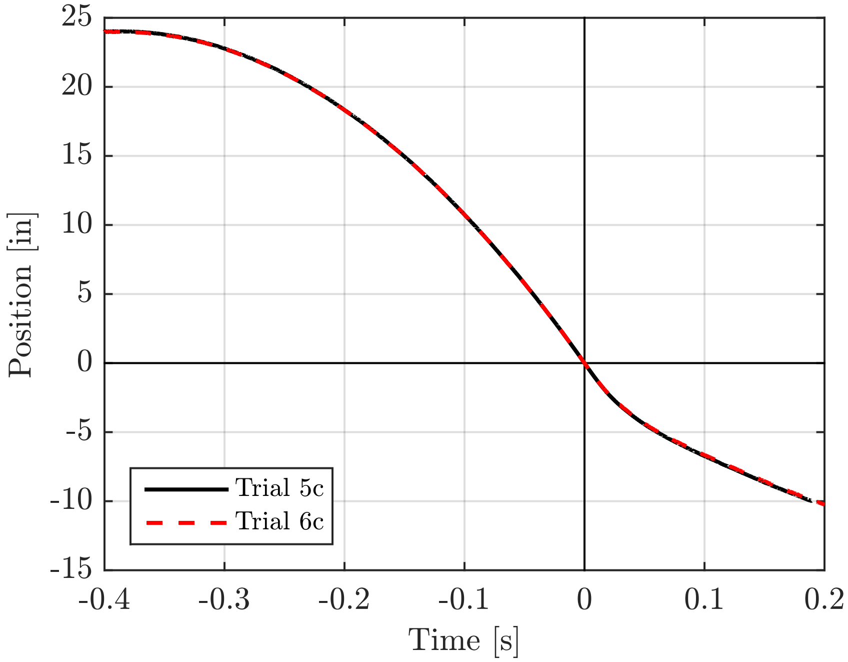

Figure 4.7: Wedge position, from drops with cameras

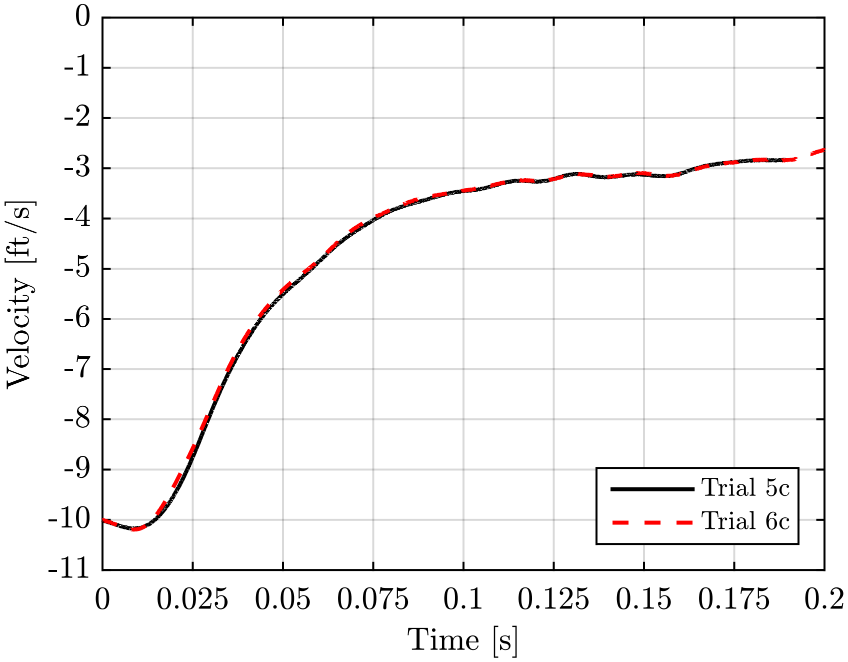

Figure 4.8: Wedge velocity, from drops with cameras

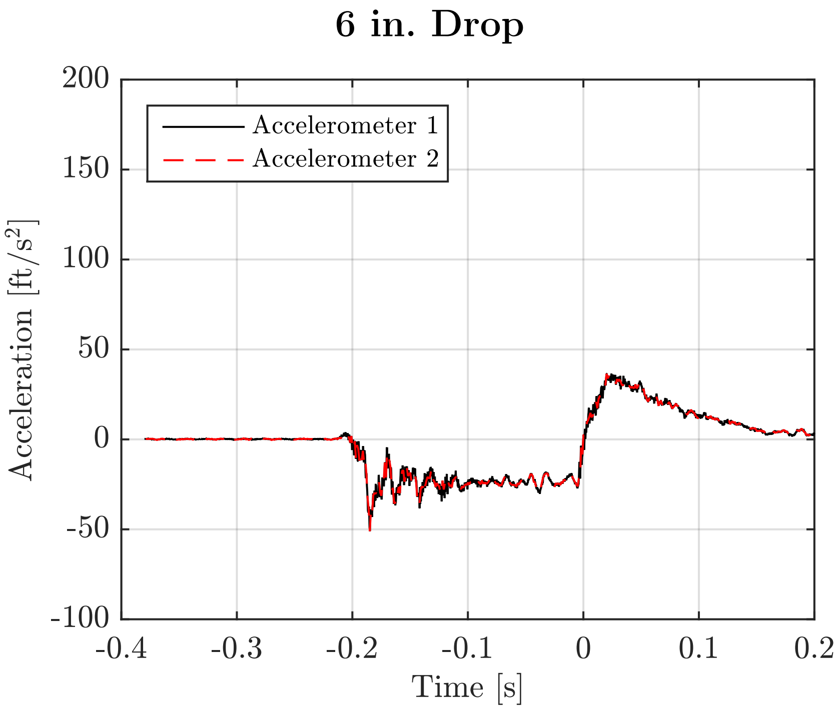

Figure 4.9: Wedge acceleration, 6 in. drop

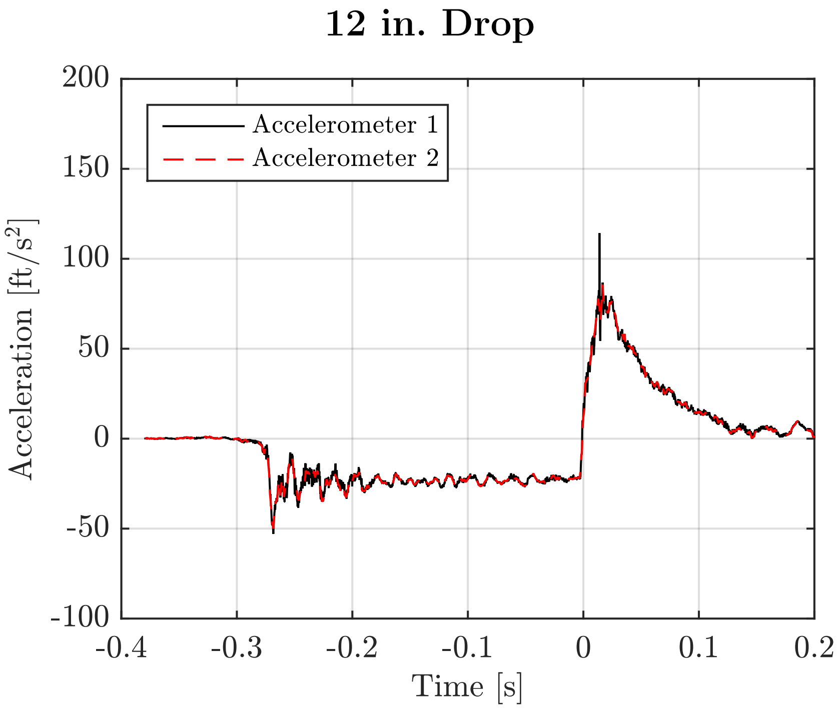

Figure 4.10: Wedge acceleration, 12 in. drop

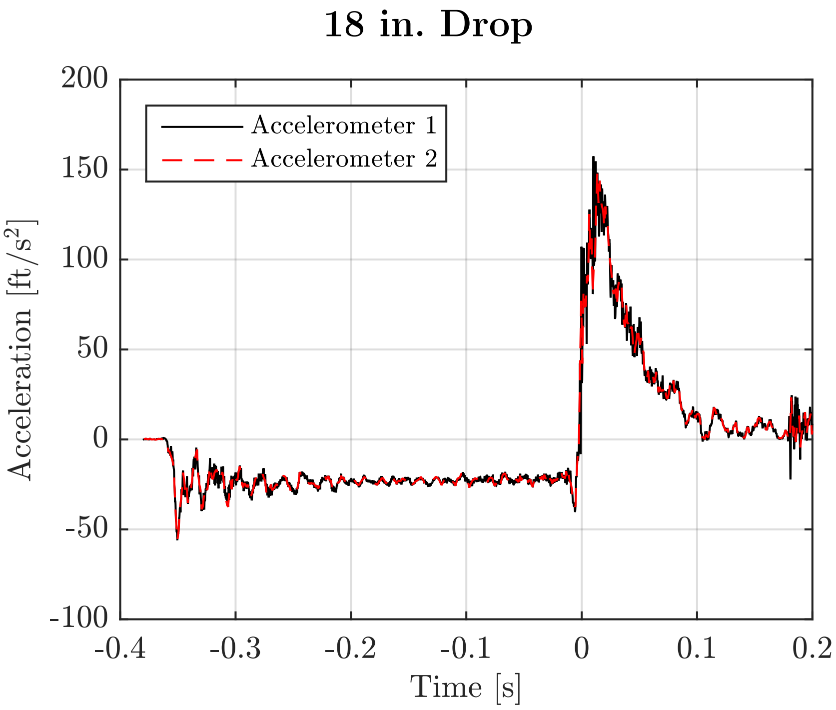

Figure 4.11: Wedge acceleration, 18 in. drop

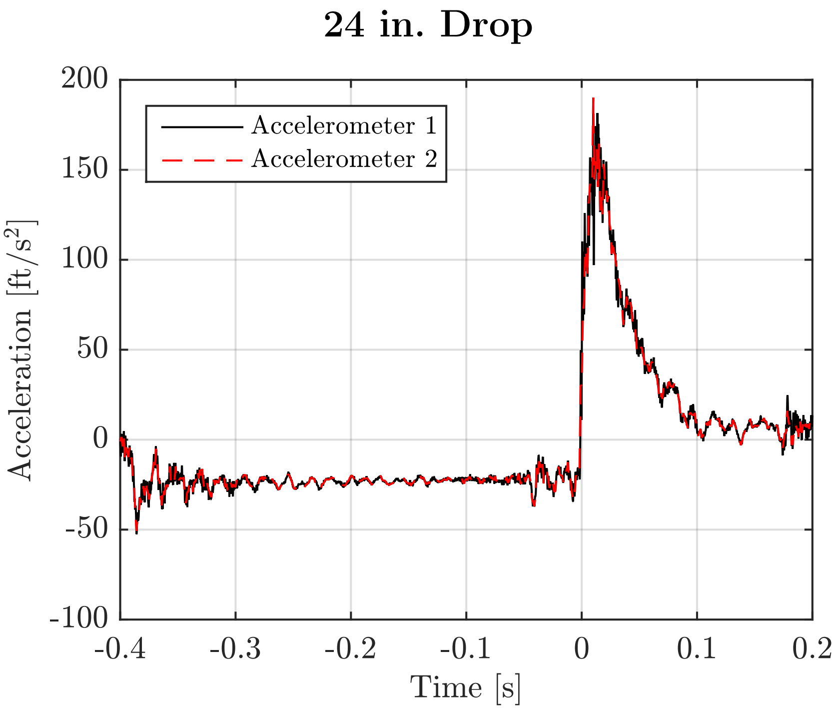

Figure 4.12: Wedge acceleration, 24 in. drop (trial 1s)

Table 4.1: Impact velocity and maximum measured strain

Quantity	Measurement	Unit
Maximum strain, trial 1s	3.582×10^{-4}	in/in
Maximum strain, trial 2s	3.692×10^{-4}	in/in
Impact velocity, trial 1s	9.701	ft/s
Impact velocity, trial 2s	9.742	ft/s
Impact velocity, trial 5c	10.011	ft/s
Impact velocity, trial 6c	10.003	ft/s

Bernoulli's Hypothesis is employed to make the necessary deadrise panel deflection calculations. The theory provides a useful relationship between vertical deflection (or panel curvature) and surface strain. This loading is analogous to the pressures induced due to the slamming event experienced by the wedge upon impact. Surface strain can also be related to the deflection by means of Bernoulli's Hypothesis and Hooke's Law. Bernoulli's Hypothesis states that plane sections remain plane in bending, and it relates strain to the bending moment by

$$\epsilon_{xx} = -zw'' \tag{4.1}$$

Here x is a longitudinal coordinate relative to the panel curvature.

Thus the panel deflection can be computed as a function of the longitudinal strain distribution by rearranging Equation 4.1, where z represents the distance between the neutral axis and the point of interest. For stresses located on the top or bottom surface of a rectangular cross section, z is equal to half the panel's thickness $t/2$. Therefore the curvature can be computed using this substitution as

$$w'' = -\frac{\epsilon_{xx}}{z} = -\frac{\epsilon_{xx}}{t/2} = -\frac{2\epsilon_{xx}}{t} \tag{4.2}$$

And the deflection can be obtained by integrating Equation 4.2 as

$$w = \iint w'' \,\mathrm{d}x\,\mathrm{d}x_1 = \iint -\frac{2\epsilon_{xx}}{t} \,\mathrm{d}x\,\mathrm{d}x_1 + c_1 x + c_2 \tag{4.3}$$

The variable x_1 is present simply to indicate that this integration will be evaluated as two integrals (one inside the other) rather than a double integral with two independent variables.

Two boundary conditions are necessary to solve for the two constants, c_1 and c_2, present in Equation 4.3. Determining the boundary conditions involves the formation of assumptions about the behavior of the panel's ends during bending, and ideally these assumptions perfectly describe the physical behavior. Zero deflection at the hard chine is chosen as the first condition due to the rigid resistance to bending provided by the wedge's side walls. The second condition is zero slope at the hard chine. These conditions effectively "fix" the panel's end at the chine though realistically any elastic panel behaves somewhere between fixed and pinned, especially when loaded dynamically during slamming events. However, it is expected that this end behaves more closely to that of a fixed end than a pinned end, so these conditions were selected and can be written as $w(x=0)=0$ and $w'(x=0)=0$ where $x=0$ at the hard chine and $x=L$ at the keel. Application of the boundary conditions to Equation 4.3 yields $c_1=c_2=0$. Numerical integration using nodes evenly spaced between the strain gages and at the beam ends is necessary to solve Equation 4.3. The numerical equation is solved for m nodes and can be written as

$$w\left(x_i\right) = -\frac{2}{t}\sum_{i=2}^{m}\left[\sum_{j=1}^{i}\epsilon_{xx,j}\Delta x_j\right]\Delta x_i \tag{4.4}$$

where $w(x_1)=w(x=0)=0$ according to the boundary conditions. Here i indexes the node for which deflection is computed and j counts the nodes from x_1 to x_i.

Wedge drop analysis in the time domain typically begins with keel impact and ends when the chine reaches the calm water level. Figures 4.5 – 4.8 show data outside these limits to demonstrate the wedge's rigid body behavior before impact and after the chine has wetted. The chine wets at approximately 0.168 sec, and the panel's maximum deflection occurs approximately 0.024 sec post-impact according to the strain gage calculations. Table 4.2 lists time domain data of the wedge's panel deflection w, vertical position z, velocity v, and acceleration a. The maximum deflections computed in trials 1s and 2s are 0.1252 in. and 0.1265 in. occurring at 0.0238 sec and 0.0239 sec, respectively.

Table 4.2: Time-dependent data: deflection, velocity, acceleration, and immersion

	Trial 1s				Trial 2s			
t [s]	w [in]	z [in]	v [ft/s]	a [ft/s^2]	w [in]	z [in]	v [ft/s]	a [ft/s^2]
0.00	0.0000	0.000	−9.6552	30.613	0.0000	0.000	−9.7420	13.571
0.01	0.0445	−1.119	−9.7375	176.561	0.0457	−1.120	−9.7207	119.388
0.02	0.1158	−2.068	−8.6847	145.161	0.1148	−2.080	−8.8009	137.388
0.024	0.1245	−2.402	−8.0741	122.449	0.1255	−2.408	−8.1596	117.502
0.04	0.1114	−3.516	−5.9802	73.527	0.1108	−3.530	−5.9777	60.656
0.06	0.0582	−4.568	−4.3702	42.402	0.0572	−4.588	−4.3411	42.096
0.08	0.0334	−5.461	−3.7190	30.870	0.0313	−5.485	−3.6831	29.022
0.10	0.0120	−6.249	−3.2964	5.267	0.0132	−6.271	−3.2944	9.315
0.12	0.0276	−6.951	−2.9275	7.612	0.0258	−6.979	−2.9922	7.339
0.14	0.0144	−7.641	−2.8122	2.762	0.0147	−7.665	−2.8207	5.813
0.16	0.0271	−8.291	−2.7596	10.054	0.0305	−8.314	−2.7196	4.381
0.168	0.0134	−8.576	−2.5933	6.938	0.0165	−8.572	−2.6270	11.852

The varying deflection distribution while stepping through time can be seen in Figures 4.13 – 4.24 and Table 4.2. This illustrates how heavily the problem depends on the wedge's location (which determines the strength of jetrise) at any given time. Note that the curves are polynomials fit to the deflection data, and each curve's vertex does not necessarily represent the maximum value calculated. An increased number of strain gages could improve this fit.

Assuming a linear relationship between deflection and surface strain allows for the estimation of an allowable deflection before the deadrise panel is over-stressed. The elastic modulus for 5086-H116 aluminum is E = 10,300 ksi and the tensile yield stress is σ_y = 30,000 psi which can be used to define a maximum allowable surface strain of the panel to be $\epsilon_{crit} = 30/10{,}300 = 29.126 \times 10^{-4}$. The estimated maximum deflection can be computed using the linear assumption and the results of maximum deflection with the associated maximum strain $\left(3.4723 \times 10^{-4}\right)$ from trial 2s as $w_{crit} = \epsilon_{crit} \times w_{max} \,/\, \epsilon_{max} = 1.0611$ in. So approximately a 1 in. deflection would be required before experiencing plastic deformation, which is eight times the deflection seen in the current experiments. Note that the surface strains observed at the moment of maximum deflection are slightly lower than the maximum surface strains occurring throughout the drop test; those strains are presented in Table 4.1.

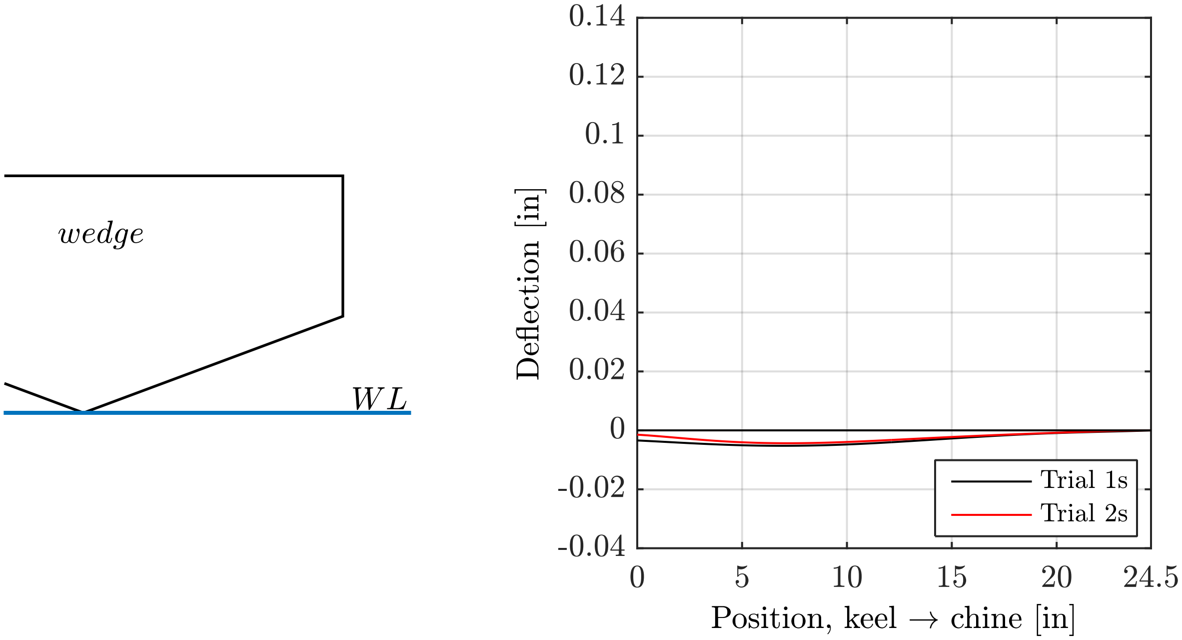

Figure 4.13: Wedge immersion and panel deflection for $t = 0.00$ s

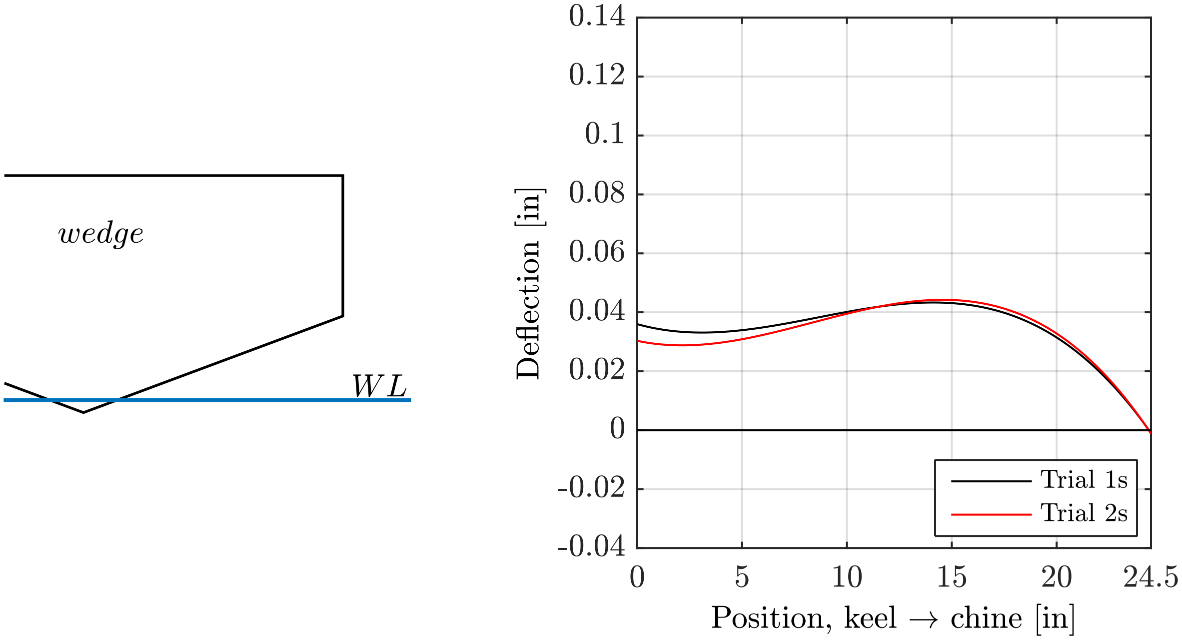

Figure 4.14: Wedge immersion and panel deflection for $t = 0.01$ s

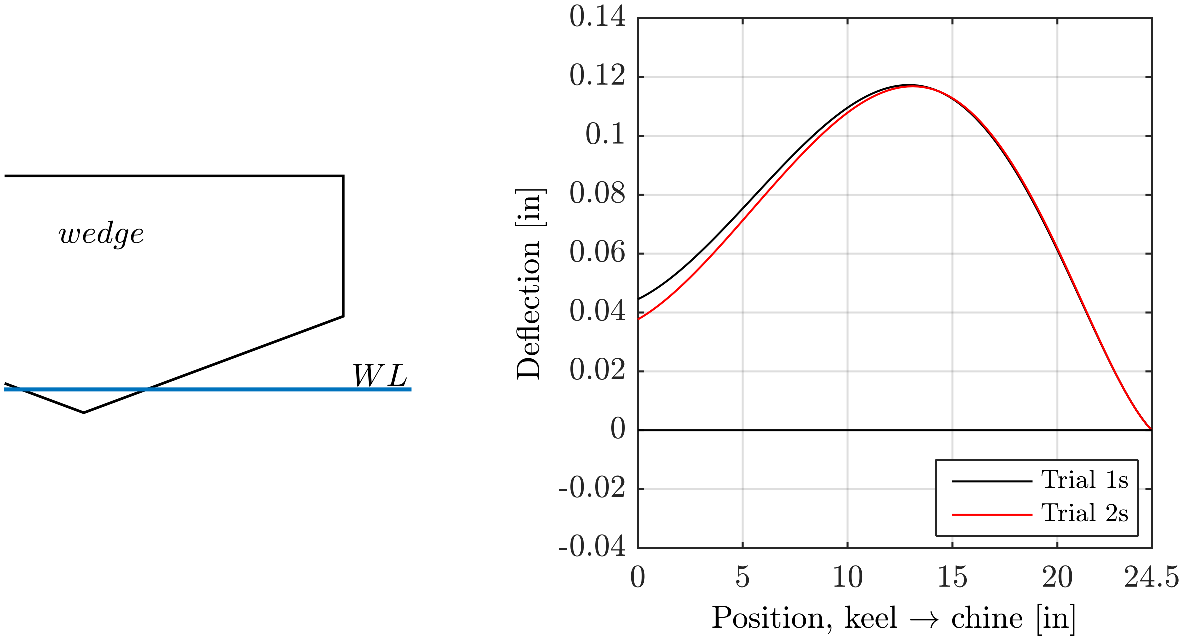

Figure 4.15: Wedge immersion and panel deflection for $t = 0.02\ s$

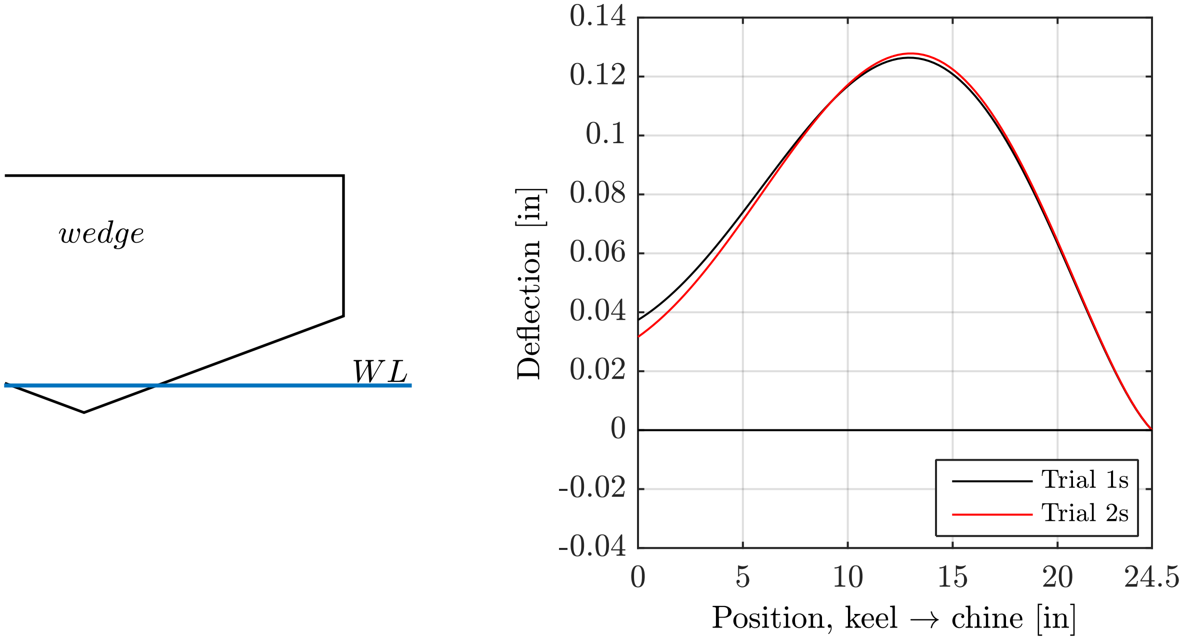

Figure 4.16: Wedge immersion and panel deflection for $t = 0.024\ s$

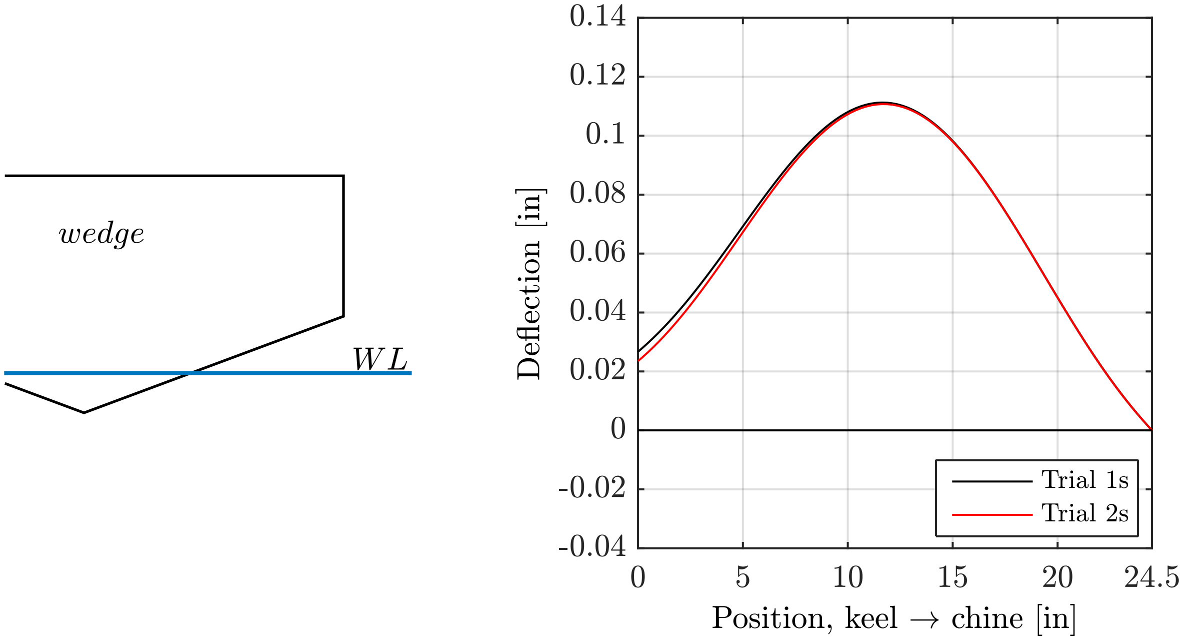

Figure 4.17: Wedge immersion and panel deflection for $t = 0.04$ s

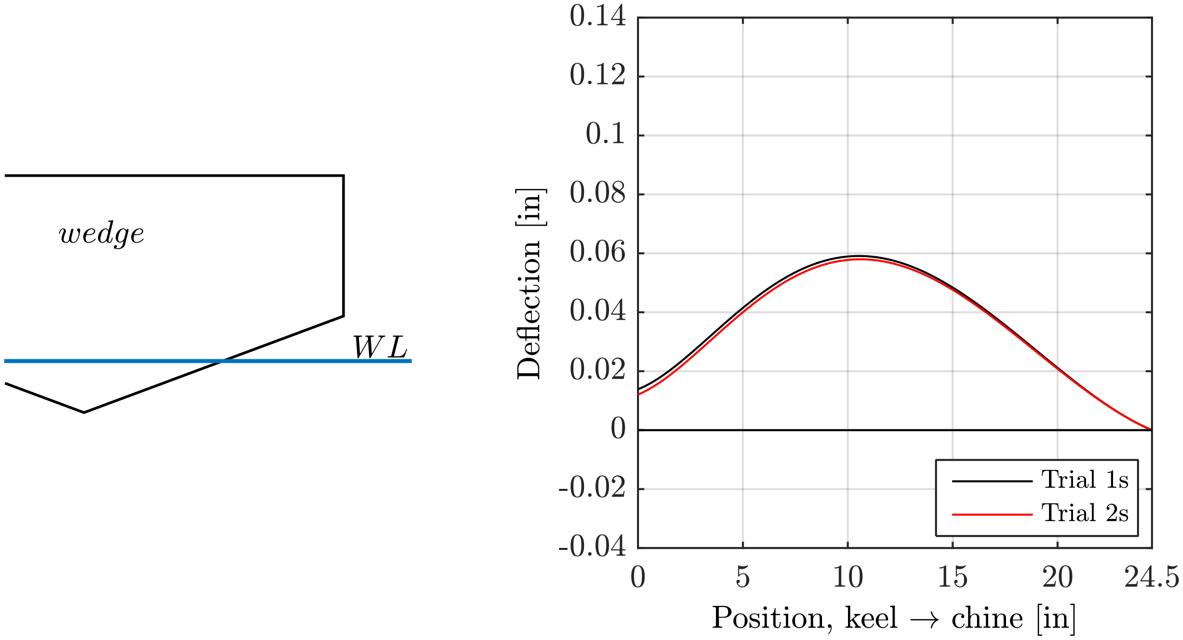

Figure 4.18: Wedge immersion and panel deflection for $t = 0.06$ s

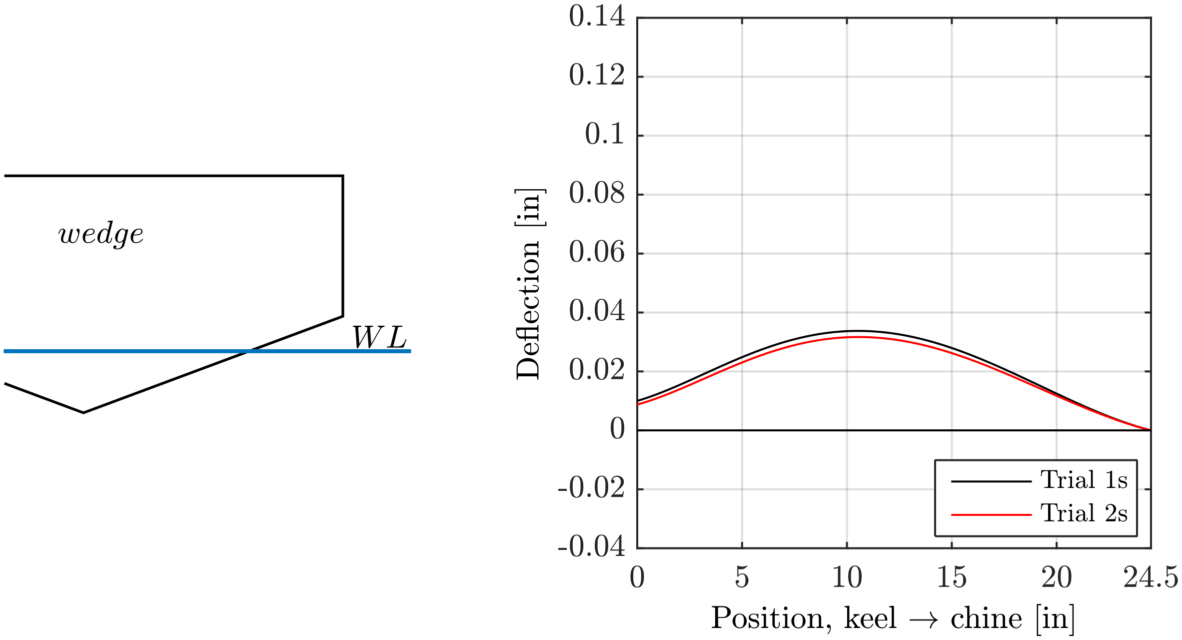

Figure 4.19: Wedge immersion and panel deflection for $t = 0.08$ *s*

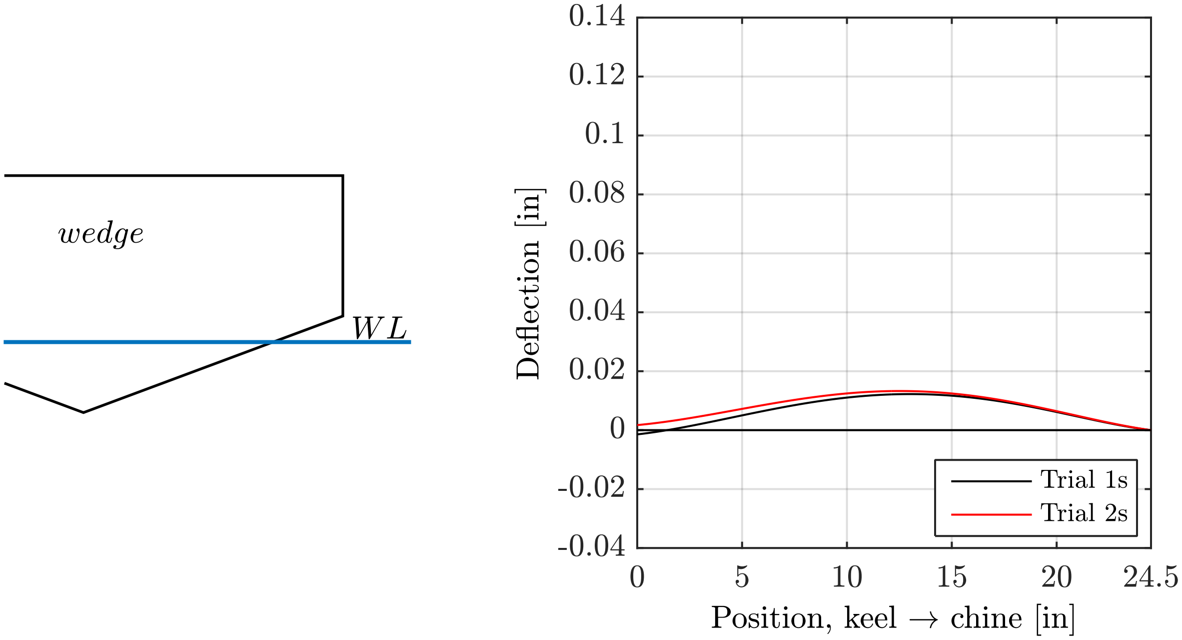

Figure 4.20: Wedge immersion and panel deflection for $t = 0.10$ *s*

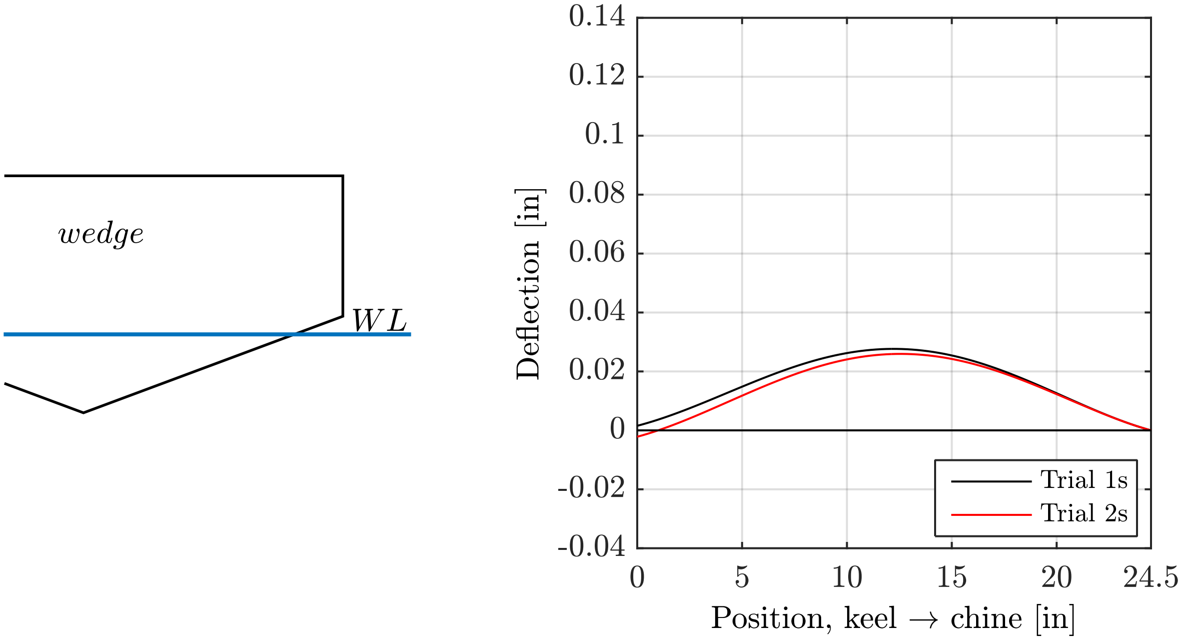

Figure 4.21: Wedge immersion and panel deflection for $t = 0.12$ *s*

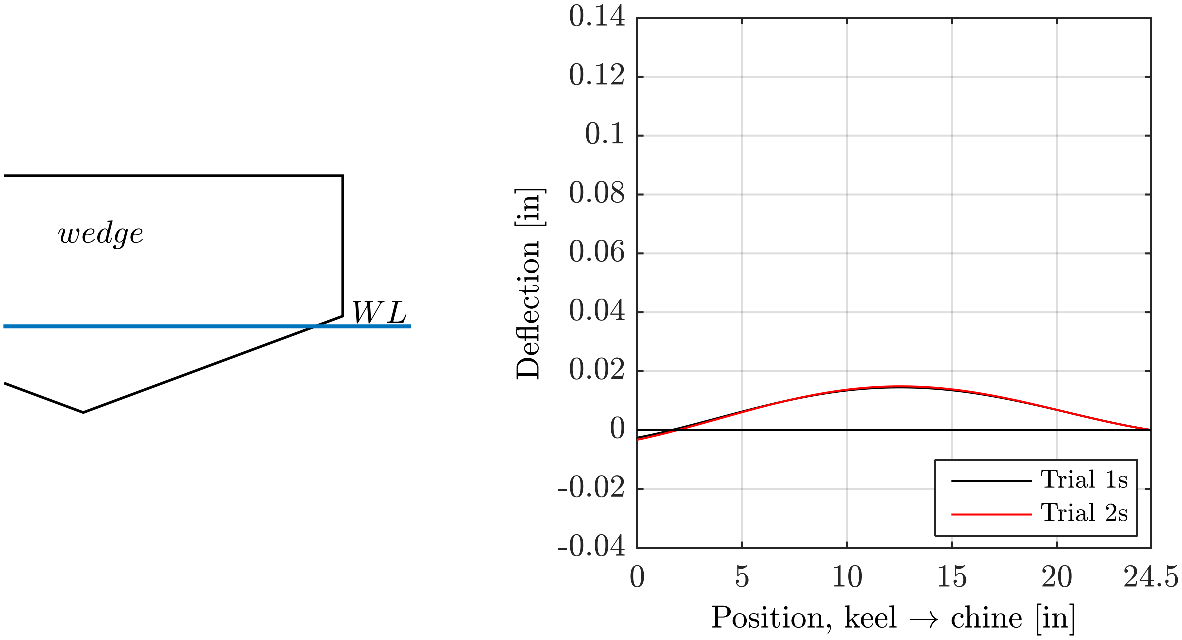

Figure 4.22: Wedge immersion and panel deflection for $t = 0.14$ *s*

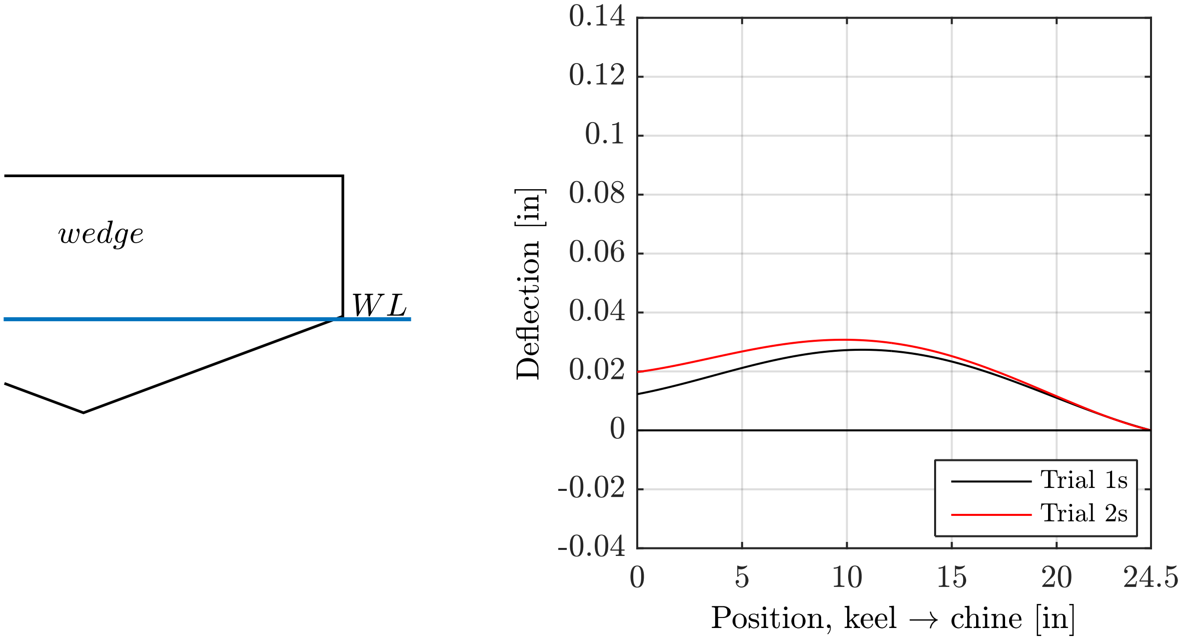

Figure 4.23: Wedge immersion and panel deflection for $t = 0.16\ s$

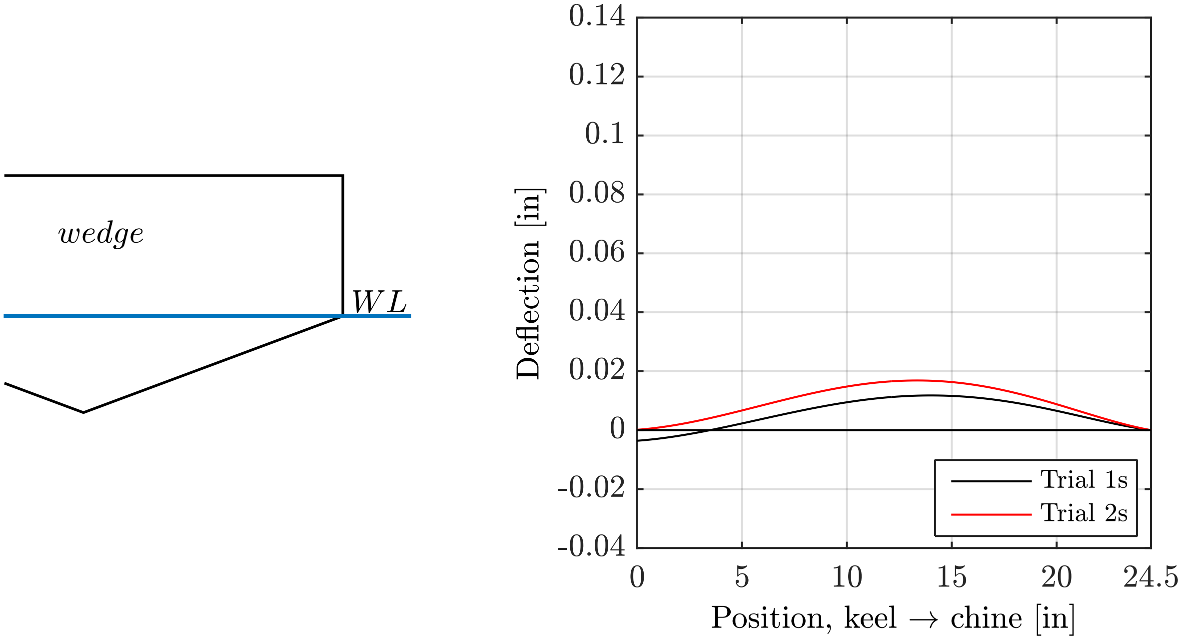

Figure 4.24: Wedge immersion and panel deflection for $t = 0.168\ s$

4.4 S-DIC Results

Two methods of handling vibration are discussed in section 3.3. After implementing Method 1 and analyzing the results, it was decided, due to the lack of dependability with the first method, to proceed with the development of Method 2. Therefore, not many results from Method 1 are available for presentation, though a maximum displacement of approximately 0.055 in. for 24 in. drops was calculated.

After the development of Method 2 was completed, the codes were tested again on the same trials (1c – 6c). This time, after processing the data, the following maximum displacements were computed: $w_{max} = 0.0970$ in. for trial 5c and 0.0879 in. for trial 6c. Figure 4.25 is a time domain plot for trial 5c including maximum deflection computed using DIC versus frame number. Table 4.3 accompanies the plot indicating the exact deflection value in each frame. Frame numbers correspond to time steps relative to impact in increments of $^1/_{\text{Sample Rate}}$, thus frame 0 was taken at impact and frame 10 was captured $^{10}/_{1400} \approx 0.00714$ seconds after impact.

The frames to be analyzed were chosen specifically to include a range surrounding maximum deflection as predicted by the strain gage calculations. Thus 30 frames were analyzed with 15 appearing before and 15 after. The curve's upward-sloping trend in Figure 4.25 indicates that more frames should have been recorded post-impact to see how the code would predict the deflection at later times and to better understand the capabilities of the method. Most of the drop test experiments were concluded before the S-DIC codes and the accompanying vibration subtraction methods were completed, therefore it was not known at the time to capture more frames post-impact. This will be accomplished in future experiments.

Table 4.3: Maximum deflection vs. frame number

		w_{max} [in]	
Time	Frame	Trial 1c	Trial 2c
0.0133	19	0.0598	0.0603
0.0140	20	0.0590	0.0636
0.0147	21	0.0572	0.0655
0.0155	22	0.0637	0.0655
0.0162	23	0.0638	0.0717
0.0169	24	0.0654	0.0684
0.0176	25	0.0751	0.0712
0.0183	26	0.0636	0.0740
0.0190	27	0.0715	0.0680
0.0197	28	0.0782	0.0728
0.0205	29	0.0813	0.0794
0.0212	30	0.0731	0.0709
0.0219	31	0.0733	0.0712
0.0226	32	0.0746	0.0734
0.0233	33	0.0751	0.0764
0.0240	34	0.0710	0.0720
0.0247	35	0.0834	0.0838
0.0255	36	0.0696	0.0798
0.0262	37	0.0784	0.0740
0.0269	38	0.0806	0.0808
0.0276	39	0.0823	0.0865
0.0283	40	0.0868	0.0918
0.0290	41	0.0914	0.0789
0.0297	42	0.0800	0.0777
0.0305	43	0.0940	0.0869
0.0312	44	0.0878	0.0965
0.0319	45	0.0970	0.0913
0.0326	46	0.0920	0.0937
0.0333	47	0.0961	0.0937
0.0340	48	0.0908	0.0880

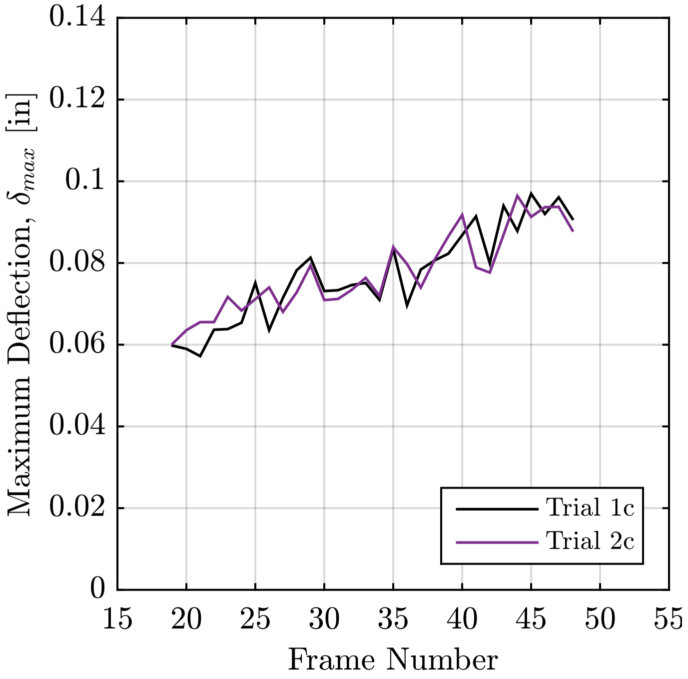

Figure 4.25: Maximum deflection vs. frame number

Chapter 5

Comparitive Study

A critical step before drawing conclusions is to compare the data obtained by both the strain gages and DIC. Cross examination is important for determining a method's reliability, and further comparison will be made possible after more trials have been performed and additional developments have been implemented. Some plots are provided to facilitate a comparison of the results. Figure 5.1 shows the deflection distribution along the deadrise panel at $t = 0.0238$ sec for trial 1s and 0.0239 sec for trial 2s. This data was interpolated with polynomials to facilitate visualizing the shape of the panel while deflected. Also plotted are the results of the DIC calculations in trials 1c – 6c. Since only a single maximum deflection is computed for each view of the panel, the largest deflections associated with each view are shown as points. The absolute maximum deflection computed using DIC occurs at 0.0319 sec in trial 5c, so the maximum values in all other DIC trials are plotted at this time step. Notice the similarity in the curves for trials 1s and 2s. The primary differences in the data are near the peak and near the wedge's keel.

Figure 5.2 is a time domain plot of maximum deflection computed using the strain gage data and DIC. Only one trial of strain gage calculations is plotted (trial 1s) for clarity. The time occurrences of maximum deflection between methods do not seem to agree. In fact, the curve's trend designating DIC results seems to slope upward indicating that possibly the maximum deflection has not yet been observed. Or perhaps the maximum deflection has indeed been observed, but an insufficient number of frames were captured to show the decline in later times.

Another time domain plot of maximum deflections is shown in Figure 5.3. Here, the deflections are computed for various drop heights including 6, 12, 18, and 24 in. For improved

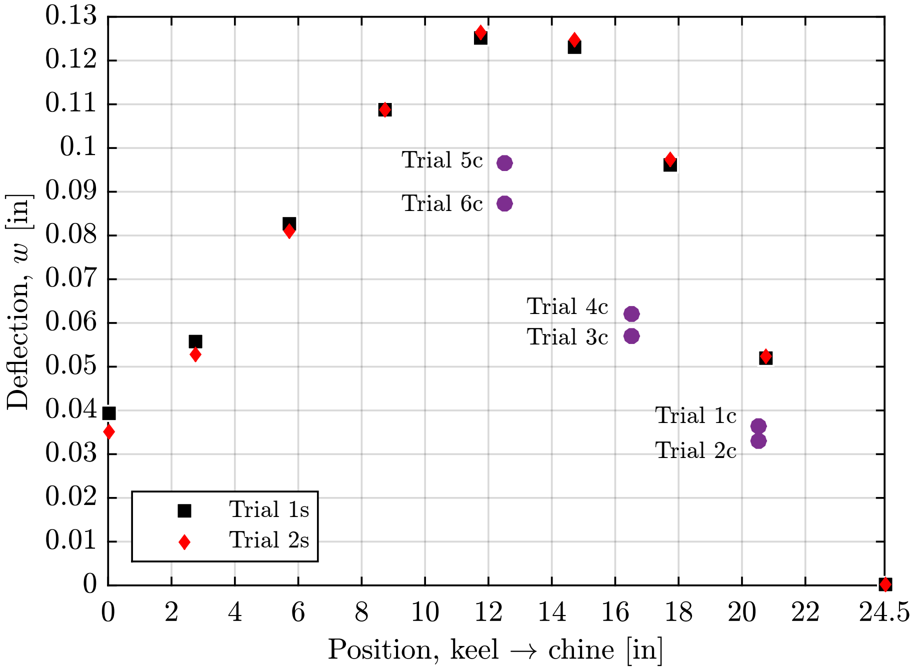

Figure 5.1: Comparison of maximum deflection versus position for each trial
The purple markers are maximum deflections found in each view in the DIC analysis

clarity, the data was interpolated to remove some of the noisy oscillations. The slope up to maximum deflection is almost perfectly linear for the 24 in. and 18in. trials. This behavior is not so evident in the data from 6 and 12 in. drop heights. The different behavior may be attributed to the changing ratio of hydrodynamic to hydrostatic pressure influences. Notice that maximum values occur at later times when reducing the drop height.

Figure 5.4 illustrates the measured pressure distribution associated with the time step, $t = 0.0238$ sec, at which the maximum deflection occurred during trial 1s. Similarly, Figure 5.5 shows the pressure distribution at the moment when maximum deflection occurred during trial 2s, 0.0239 sec. Included in both plots are the corresponding theoretical pressure distributions as predicted by Taravella [16]. Some similarity is evident in the shape of the curves as well as the maximum values (the peaks appearing near the 10 in. location). Coincidentally, a pressure sensor was placed at almost exactly the same location where the maximum occurs as predicted by the theoretical code. Sensor 4 is located at 10.23 in., and the maximum predicted pressure occurs at 10.47 in.

Table 5.1: Summary of measured data for trials with strain gages

		Drop height			
Measurement	Units	6 in	12 in	18 in	24 in
Impact velocity	ft/s	4.812	6.789	8.383	9.742
Maximum pressure	psi	3.998	7.425	10.804	13.989
Maximum deflection	in	0.051	0.078	0.105	0.125
Maximum acceleration	ft/s^2	40.72	114.55	157.78	193.67

A third comparison plot of pressure versus position was made and can be seen in Figure 5.6. Specifically, the time step, 0.0231 sec, at which the code's predicted maximum pressure occurs directly at 10.23 in. from the keel is plotted. Better agreement between the measured and theoretical peaks can be observed indicating that the pressure near the spray root jet is predicted fairly accurately. The plotted theoretical curve includes the hydrostatic component of pressure which shifts the data near the keel up very slightly. Obviously, since the peak occurs at the free surface, the hydrostatic influence is zero.

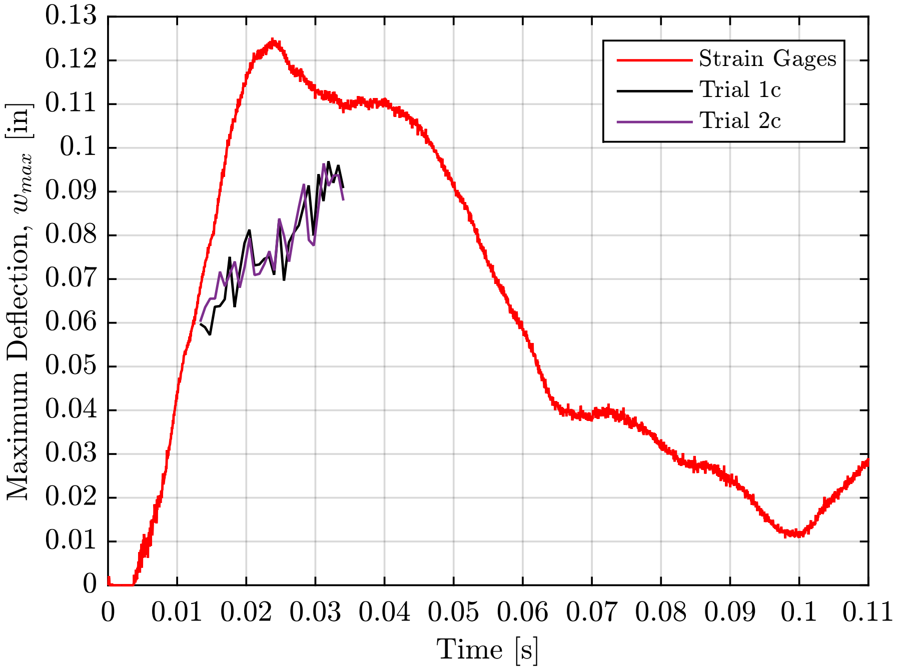

Figure 5.2: Maximum deflection versus time, comparison

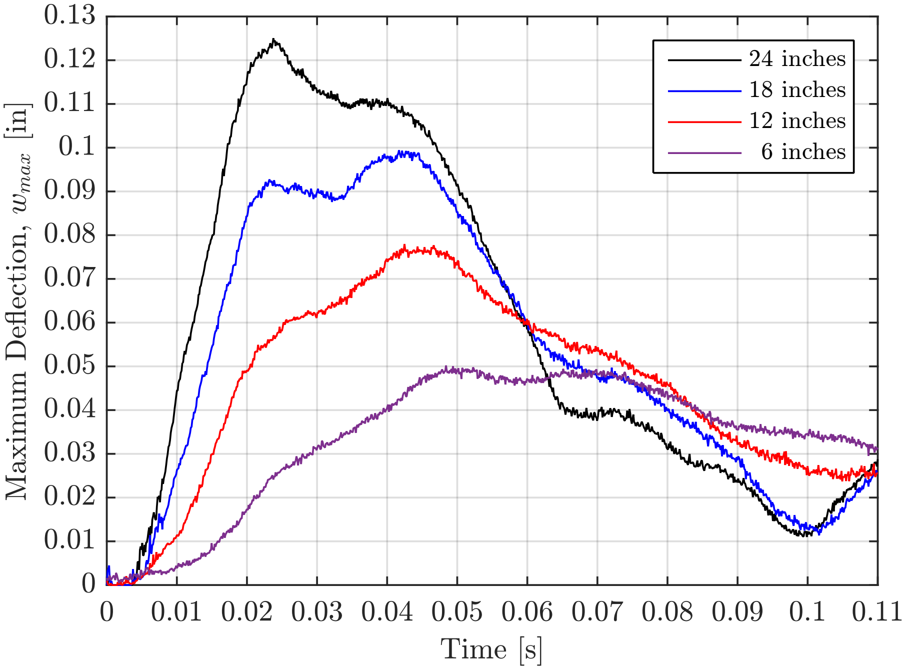

Figure 5.3: Maximum deflection versus time for various drop heights

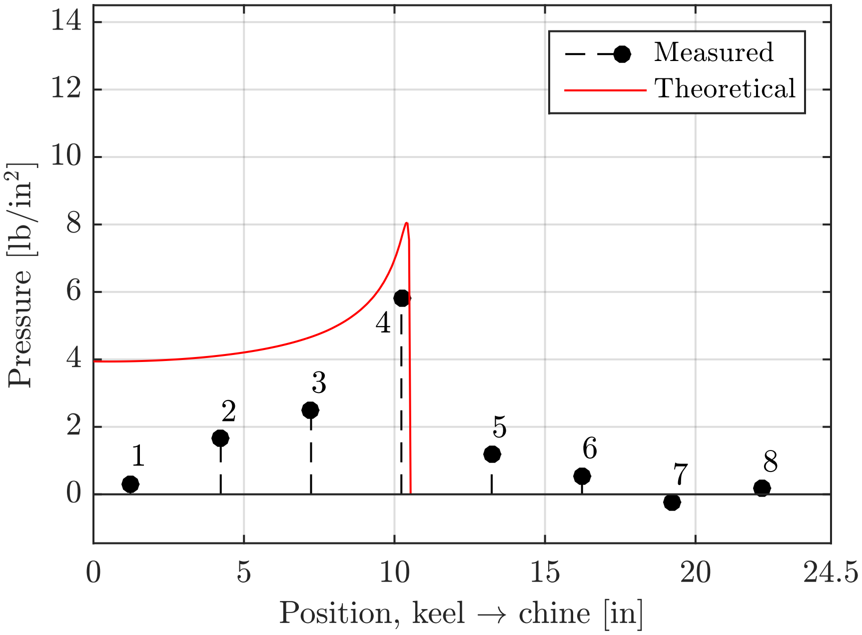

Figure 5.4: Pressure distribution along panel at $t = 0.0238$ s, trial 1s

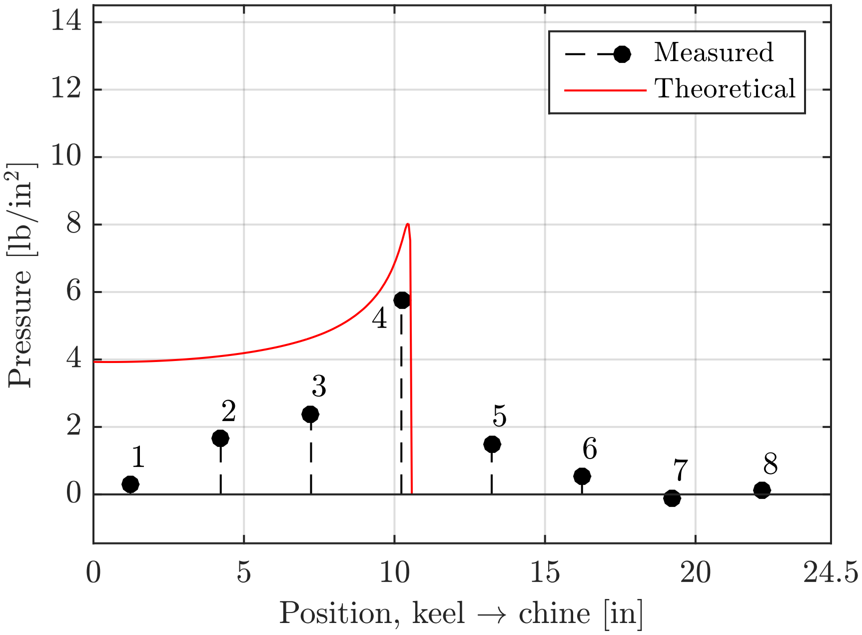

Figure 5.5: Pressure distribution along panel at $t = 0.0239$ *s, trial 2s*

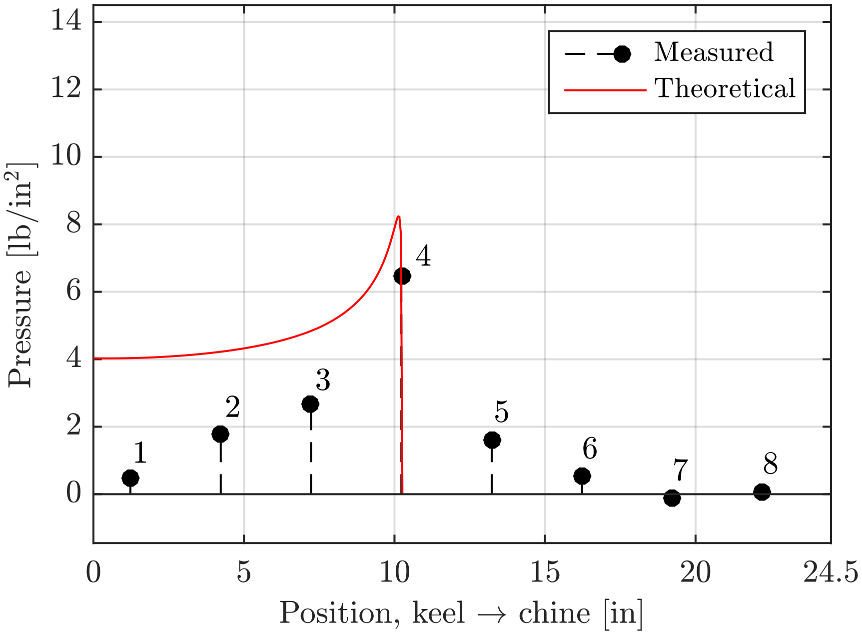

Figure 5.6: Pressure distribution along panel at $t = 0.0231$ *s, trial 1s*

Chapter 6

Conclusions and Future Work

In this study, the hydroelastic response of an elastic aluminum wedge model due to wave slamming effects is investigated. Emphasis is placed on two items: the use of strain gages to analyze deadrise panel deflections, and the development of a Stereoscopic-Digital Image Correlation code to advance the capabilities of future research. The goal is to learn more about the importance of hydroelasticity in shell plating on planing vessels experiencing wave slamming at high speeds. Specifically, it is of interest to know its influence in a vessel's seakeeping characteristics as this can drastically reduce the hull's efficiency in terms of resistance or even produce unsafe accelerations for onboard personnel and provisions. Some researchers [4, 14, 18] have hypothesized that the elastic deflections of a vessel's shell plating may in fact reduce the vertical impact accelerations by absorbing a portion of the vessel's kinetic energy in its descent. Increasing hydrodynamic pressures due to jetrise from greater impact velocities predict a contrary outcome. These issues will be discussed in context of the present experimental results.

Based on the deflection calculation results and comparisons shown in chapters 4 and 5, it is concluded that greater reliability is found in the calculations made with the strain gage data. Drop tests with varying drop height were carried out and the data was analyzed to justify this conclusion. Therefore, the strain gage results are used in making conclusions about hydroelasticity and the comparisons from chapter 5. Future reports are expectant which will provide more data for different drop heights and panel thicknesses, especially concerning the developments and implementation of the Stereoscopic-Digital Image Correlation technique. Much room for improvement lies within the calculations made using S-DIC, and some suggestions are discussed in section 6.2.

6.1 Hydroelastic Response

Panciroli [11] concluded that the effects of deadrise panel deformations on hydrodynamic pressure are negligible until the time of maximum impact force. In the present investigation, the maximum impact forces are seen where the magnitude of the wedge's acceleration – or more precisely, deceleration – is highest, around 0.01–0.04 sec. And the highest recorded pressures are also in this time frame (see Figures 4.1 – 4.4 and Figures 4.9 – 4.12). However, Figure 5.2 and Table 4.2 reveal that the panel deflection has not yet reached even one-third its maximum value at 0.01 sec post-impact, and by the time of maximum deflection, the span-wise hydrodynamic pressure distribution has diminished to the smaller values as shown in Figures 5.4 and 5.5. Thus it appears that the panel deflections are associated more with the shape of the pressure distribution rather than its magnitude at certain locations.

As previously discussed in chapter 1, Vorus [18] incorporated variable contour shapes into his analysis. Three particular contours were used, one designated as 20–10, one as 20–20, and a third as 20–30. The two numbers in his convention indicate initial deadrise at the keel and terminating deadrise at the hard chine, respectively. When using Vorus' polynomials defining the contour shape, the maximum deflection of a 20–10 shape can be computed as

$$\left(\frac{w_{max}}{\ell}\right)_{\text{20-10}} = 0.0211 \tag{6.1}$$

where ℓ is the length of the panel spanning from the keel to the chine [18]. Thus 0.0211 is the non-dimensional maximum deflection when normalized on the panel length. Studies of the flow physics were analyzed numerically with this contour simulating the response of a vessel designed with cambered panels. The corresponding deflection for the current wedge is computed as $w_{max} = 0.0211 \times 24.50 = 0.5170$ in. Vorus' study included the assumption that the 20-10 contour acted as the resting (unloaded) yet rigid shape of a panel, and his calculations were made with the associated body boundary conditions. Note that even though Vorus' contour represents a panel with much greater curvature than the current panel in its moment of greatest deflection, the stresses on his panel are still only half the yield stress according the linear assumption as discussed on page 49. This indicates that the panel deflections could increase by a factor of eight without over-stressing the material.

Less than 0.13 in. deflections were observed in the present investigation of an unstiffened flat panel. Displacements of greater magnitude than this are unlikely to be observed in *flat* shell plating of high speed marine vessels due to the necessary plate stiffening. Wave slamming on unstiffened plating is considered too dangerous and threatening of failure and plastic deformation. So Vorus' study of varying panel contours seems to be relevant only for the analysis of cambered panels; the deflections presently observed in flat panels are not great enough to be comparable with Vorus' 20–10 contour. The 20–10 and 20–30 contours represent cambered shapes that may be part of the vessel's design near areas of steep gradients, but it is unlikely that hydroelastic effects will produce similar loading. While naval architects generally avoid the incorporation of high gradients in shell plating contours for ease of construction and improved overall hydrodynamic performance, some planing vessels do have regions of high curvature near hard chines to facilitate the generation of lift on the approach to planing speeds. The designer must be careful, though, because wave slamming forces are known to dramatically and quickly reduce a vessel's forward speed [14].

Further analysis of the hydrodynamic pressures and the wedge's vertical motions leads to additional conclusions. When the drop height is quadrupled from 6 in. to 24 in., the deflections only slightly more than double from 0.051 in. to 0.126 in. The maximum acceleration for a 6 in. drop height is ~40.7 ft/s and ~193.7 ft/s for 24 in. drops. This represents an increase in acceleration by a factor of over 5.27. The maximum measured hydrodynamic pressures increase almost perfectly linearly while incrementally increasing the drop height as shown in Figure 6.1, and this is expected in a rigid plate since pressure is proportional to the impact velocity squared in dynamic problems [16]. An increase by a factor of just over 3.64 is observed between 6 in. and 24 in. heights, indicating that the increase is almost quadrupled like the drop height.

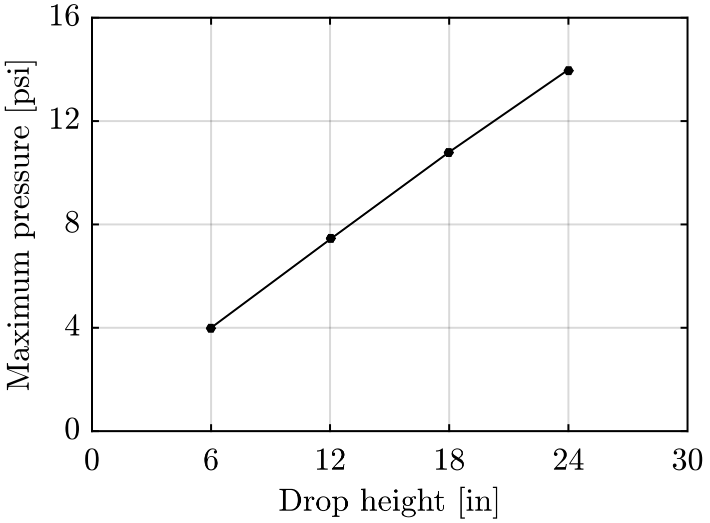

Figure 6.1: Maximum pressure versus drop height trend

It is therefore concluded that the deflections found in the flat shell plating of marine vessels are not great enough in magnitude to significantly alter the flow physics governing their hydrodynamic performance and seaworthiness. Improvements in these studies will lead to a better understanding of the hydroelastic characteristics of ships, and further developments can be made in the validation of analytical codes with future improvements to the present DIC and strain gage analyses.

6.2 Future Work

The assumption made in subsection 3.3.2 regarding time step correspondence between drop test trials was considered to be valid, and this was necessary in order to legitimize the calculations. However, observation of Figure 5.2 leads to the conclusion that this assumption is not completely credible considering the fluctuations in the DIC trend. Deadrise panel deflections vary dramatically with time, as illustrated in the incrementing of time between plots in Figures 4.13 – 4.24, because the time-dependent variables (e.g. wedge vertical velocity and hydrodynamic pressure) are quite sensitive to the passage of time. Therefore it is necessary to attenuate the vibratory displacements occurring between the cameras and wedge as much as possible. Also, relative motions between the two cameras can cause erroneous calculations, making the reduction of any undesired motions even more critical.

Numerous ideas are being developed to reduced the troublesome relative motions that the stereo cameras are experiencing. Executing these improvements and accomplishing successful wedge drops with reduced relative motions between the wedge/camera system is expected. This would ideally remove the necessity of utilizing the presently necessary vibration removal routines, and thereby improving the accuracy of the triangulation calculations.

Further DIC code developments and added experience with image processing and capturing high speed video should also warrant another attempt with the speckle pattern. Achieving greater clarity and diminished motion blur with reduced system vibration is also possible. This will allow for the observation of finer details in the strain field and displacements. Correlation template sizes can also be adjusted more readily with small random speckles than a checkerboard pattern.

Alternatively, it would be of interest to extend the use of the checkerboard pattern in observing deflections over the full span of the deadrise panel. Either different camera lenses will need to be used or more views will be added to the analysis in order to accomplish this task. A desirable result of this extension will be obtaining a deflection distribution over the entire span of the panel as well as distributions at various longitudinal positions. Then the keel deflections as predicted by the strain gages can be validated. Static methods of validating both the strain gage and S-DIC calculations is desirable as well. This could be done e.g. by elastically loading a beam and measuring the deflection with the strain gages, S-DIC, and a simple ruler with marks indicating the unloaded and deformed positions. This should further add confidence to the experimental methods.

More strain gages and equipment for collecting data have recently been acquired. This will permit the use of up to 16 strain gages in future testing, thus enabling a refinement of the strain distribution along the deadrise panel. It may be found that adding more colinear nodes is unnecessary, in which case the additional equipment will be used to collect data at a second longitudinal position providing more details of the three dimensional effects. Both of these arrangements are to be tested regardless.

It is also important to consider the repeatable nature of the strain gage calculations. Minimal differences are present in these results unlike DIC. Figure 5.1 further illustrates this point. Both distribution curves obtained from the strain gage data are almost identical with the comparably insignificant exception of keel deflections. The points plotted from the S-DIC calculations appear to diverge while approaching midspan from the hard chine, but this disparity will expectantly improve. Further trials with the same wedge and also with different models are scheduled for testing and will be used to perform additional studies in hydroelasticity. A deadrise panel with reduced thickness should see greater deflections making it easier to study the similarities and differences between the strain gage and Stereoscopic-Digital Image Correlation methods, so a new wedge with $^3/_{16}$ in. thick panels is to be tested. Relationships between the wedge's vertical motions, hydrodynamic pressures, and deadrise panel deflections should lead to additional conclusions about the significance of hydroelasticity in the declination or improvement of global acceleration and resistance characteristics of planing vessels.

References

[1] Alsamman, A. R. “Digital Image Processing” 2016. Lecture Notes, University of New Orleans.

[2] Bebis, G. “Computer Vision” 2004. Lecture Notes, University of Nevada. Online; accessed 11-November-2016. `https://www.cse.unr.edu/~bebis/CS791E/`

[3] Biggs, D. S. C. “Acceleration of Iterative Image Restoration Algorithms” (1997). *Applied Optics, Vol 36*(8), pp 1766–1775.

[4] Faltinsen, O. M. “Water Entry of a Wedge by Hydroelastic Orthotropic Plate Theory” (1999). *Journal of Ship Research, Vol 43*(3), pp 180-193.

[5] Gimel’farb, G. “Intelligent Vision Systems” 2016. Lecture Notes, University of Auckland. Online; accessed 11-February-2016.
`https://www.cs.auckland.ac.nz/courses/compsci773s1c/lectures/`

[6] “Hosseini, A., Mostofinejad, D., and Hajialilue-Bonab, M. “Displacement Measurement of Bending Tests Using Digital Image Analysis Method” (2012). *IACSIT International Journal of Engineering and Technology, Vol 4*(5), pp 642-644.

[7] Ikeda, C. “Deflections on the Bottom of a Wedge-Shaped Hull due to Slamming Loads” (2915). *Transactions, Vol 123*, SNAME.

[8] Ikeda, C., Ghandehari, P., Castro F., Aucoin C., Bye B. “Slamming load effects on the bottom of high-speed aluminum planing craft” (2015). 13th International Conference on Fast Sea Transportation.

[9] Judge, C., Troesch, A., and Perlin, M. “Initial water impact of a wedge at vertical and oblique angles” (2004). *Journal of Engineering Mathematics, Vol 48*, pp 279-303.

[10] Lyon, R. F. “The Optical Mouse: Early Biomimetic Embedded Vision” (2014). *Advances in Embedded Computer Vision.* Springer, pp 3-22.

[11] Panciroli, R. “Hydroelastic Impacts of Deformable Wedges” (2012). Ph.D. dissertation, University of Bologna.

[12] Peterson, R., Wyman, D., and Frank, C. “Drop tests to support water-impact and planing boat dynamics theory” (1997). CSS Technical Report 97, Coastal Systems Station, Panama City, Florida.

[13] Quintana, E., Reu, P., Jimenez, E., and Thompson, K., and Kramer, S. “Digital Volume Correlation for Materials Characterization” (2016). 19th World Conference on Non-Destructive Testing.

[14] Royce, R. A. “2-D Impact Theory Extended to Planing Craft with Experimental Comparisons” (2001). Ph.D. dissertation, University of Michigan.

[15] Savander, W. S. “Steady Hydrodynamic Analysis of Planing Surfaces” (2002). *Journal of Ship Research, Vol 46*(4), pp 248-279.

[16] Taravella, B. M. Program for computing analytical wedge drop results (2016). In-house computer program, University of New Orleans.

[17] Von Kármán, T. H. “The impact on seaplane floats, during landing” (1929). NACA Technical Note 321, Washington, D. C.

[18] Vorus, B. R., Scorpio, S. M., and Taylor, R. K. “A Flat Cylinder Theory for Vessel Impact and Steady Planing Resistance” (1996). *Journal of Ship Research, Vol 40*(2), pp 89-106.

[19] Wagner, H. “Über Stoß-und Gleitvorgänge an der Oberfläche von Flüssigkeiten” (1932). *Zeitschrift für Angewandte Mathematik und Mechankik, 12*(4), pp. 193-215.

Vita

Jonathan Eastridge is from Clover, South Carolina and is the younger of two sons to Tom and Laura Eastridge. He moved to New Orleans to study Naval Architecture and Marine Engineering at the University of New Orleans in August, 2013 and graduated with honors in May, 2016. Upon completion of his master's degree in May, 2017, Jonathan hopes to continue his education in pursuit of a Ph.D. in Engineering and Applied Science at UNO.